Degradation and Failure Analysis of Environmental Barrier Coatings under Adverse Operating Environment: Multi-physics Modelling

Rajan Suwal

Thesis submitted to the University of Ottawa
in partial fulfillment of the requirements for the
Master of Applied Science degree in Mechanical Engineering

Department of Mechanical Engineering
Faculty of Engineering
University of Ottawa

Abstract

Environmental barrier coatings (EBCs) are essential for protecting ceramic matrix composite (CMC) substrates in advanced gas turbines and aero-engines. However, their durability is limited by thermo-mechanical stresses, oxidation, and water-vapor-induced degradation under high-temperature operating conditions. The premature failure of EBCs, particularly delamination along the interfaces of thermally grown oxide (TGO) poses major challenges to coating reliability. This research presents a systematic study of the degradation of bi-layer $Yb_2Si_2O_7$/Si EBCs using COMSOL Multiphysics methodologies. Thermal cycle-induced temperature fields were implemented into the EBC model, aiming to simulate the system's in-service conditions. Coupled thermo-mechanical processes were simulated, incorporating high-temperature creep behavior, phase transformation from $Yb_2Si_2O_7$ to Yb_2SiO_5, and TGO growth kinetics. The model also accounted for the β–α phase transformation of cristobalite TGO between 220°C and 270°C, which introduces significant volumetric changes during cooling. Based on the evaluated local stress evolution and distribution in the EBC system during thermal cycles in water-vapor environments, the experimentally observed EBC degradation mode was explained in terms of the simulated results. Fracture behavior was investigated using J-integral, Virtual Crack Extension, and a phase-field damage model to capture crack initiation and propagation within the coating system. The results show that large tensile stresses in the TGO promote spontaneous crack formation, which can bifurcate and propagate along $Yb_2Si_2O_7$/TGO and Si/TGO interfaces. Coalescence of these bifurcation-induced delamination cracks could be the primary mechanism leading to the EBC's spallation and failure. The simulated TGO crack growth pattern was compared with that experimentally observed in the literature. Additionally, the effect of interface morphology on crack evolution was systematically investigated. Increasing interface undulation was found to intensify local stress concentrations, enhance mixed-mode fracture driving forces, and accelerate interfacial delamination. The findings of this study enhance the understanding of EBC degradation and provides an integrated multi-physics framework for predicting failure.

Acknowledgements

First and foremost, I would like to express my deepest gratitude to my supervisor, Dr. Arnaud Weck, for his invaluable guidance, continuous support, and encouragement throughout this research. I am also profoundly grateful to my co-supervisor, Dr. Kuiying Chen from the National Research Council Canada, for his invaluable discussions, technical assistance, and for fostering a stimulating and collaborative research environment. Their expertise, patience, and insightful feedback have been instrumental in shaping both the technical and conceptual aspects of this work.

This work was made possible through funding from the National Research Council Canada (NRC), the Natural Sciences and Engineering Research Council of Canada (NSERC), and the Ontario Graduate Scholarship (OGS), whose generous support I sincerely acknowledge.

I would also like to extend my appreciation to the members of my research group for their valuable feedback and support, which made this journey both productive and enjoyable.

Finally, I am deeply thankful to my family and friends for their unwavering encouragement, patience, and understanding throughout my studies. I wish to express my heartfelt gratitude to my wife, Sahara, for her endless love, support, and encouragement, which have been my constant source of strength and motivation throughout this journey.

This thesis stands as a reflection of the collective efforts, guidance, and inspiration I have received, and I dedicate it to all who contributed to this journey.

Table of Contents

List of Figures

List of Tables

List of Acronyms

AMR — Adaptive Mesh Refinement

APS — Atmospheric Plasma Spray

BSAS — Barium Strontium Alumino-Silicate

CMAS — Calcium–Magnesium–Alumino–Silicate

CMC — Ceramic Matrix Composite

CTE — Coefficient of Thermal Expansion

CZM — Cohesive Zone Model

EBC — Environmental Barrier Coating

FEM — Finite Element Method

FOD — Foreign Object Damage

PFM — Phase-field model

RE — Rare Earth

SEM — Scanning Electron Microscopy

SIF — Stress Intensity Factor

Si — Silicon

SiC — Silicon Carbide

SiO_2 — Silica

TIT — Turbine Inlet Temperature

TBC — Thermal Barrier Coating

TGO — Thermally Grown Oxide

VCCT — Virtual Crack Closure Technique

VCE — Virtual Crack Extension

XFEM — eXtended Finite Element Method

Yb_2SiO_5 — Ytterbium Monosilicate

$Yb_2Si_2O_7$ — Ytterbium Disilicate

1. Introduction

As the aerospace and energy sectors strive for higher efficiency, reduced emissions, and improved power-to-weight ratios, the thermal and mechanical demands of turbine engines have increased significantly. Nickel-based superalloys, which have traditionally been used in turbine components, are approaching their performance limits, particularly in advanced engine designs operating at elevated temperatures. Ceramic matrix composites (CMCs), particularly SiC/SiC composites, have emerged as promising candidates for hot-section components in gas turbines due to their high specific strength and stiffness, excellent oxidation resistance, and superior mechanical performance at elevated temperatures [1], [2], [3], [4]. However, when exposed to service conditions in gas turbines, CMCs are subjected to severe environments involving high temperatures, reactive gases, and complex stress states, which can compromise their durability. To mitigate these challenges, environmental barrier coatings (EBCs) have been developed, serving a role similar to that of thermal barrier coatings (TBCs) on metallic superalloys by protecting CMC surfaces from environmental degradation [5], [6].

Protective coatings are critical for extending the service life of hot-section components and enhancing turbine efficiency by allowing operation in adverse environments. Many studies have focused on TBCs deposited on superalloy substrates. For example, Marcin [7] investigated thermal stress distribution in YSZ/NiCoCrAlY coatings on nickel-based superalloys using finite element analysis, including the effect of delamination cracks. Wang et al. [8] studied the thermal residual stresses in $La_2Zr_2O_7$/8YSZ coatings using the birth–death element method to simulate service-like conditions and examine crack formations. Other studies have examined the effect of thermally grown oxide (TGO) thickness [9], interface roughness [10], [11], and porosity [12] in TBCs.

The growing interest of CMCs in turbine applications has shifted attention toward EBCs. The materials system and failure mechanisms for CMCs differ significantly from those of conventional superalloys. The long-term durability of EBC systems depends not only on their resistance to environmental degradation but also on their ability to withstand the complex mechanical and thermal stresses encountered during service. These stresses, particularly those arising from interactions between EBC materials and the environment during thermal cycling, can lead to cracking, delamination, and eventual coating failure.

Several studies have examined residual stress development in these coatings. Lee et al. [13] analyzed the thermal residual stress of a Si/mullite ($3Al_2O_3 \cdot 2SiO$)/barium strontium alumino-silicate (BSAS) coating deposited on SiC/SiC composites. Richards et al. [14], [15], [16] investigated the properties and failure mechanisms of ytterbium silicate–based EBCs, suggesting that TGO growth, deposition conditions, and microstructural defects strongly influence coating lifetime. The finite element method has been utilized to evaluate the residual stress of EBC systems on SiC/SiC composites [17], [18]. Other finite element studies have emphasized the role of interfacial roughness in generating stress concentrations [19], coating thickness on energy release rate and interfacial crack initiation/propagation [20], and water-vapor-induced phase transformations in accelerating cracking and delamination [21]. More recently, Cheng et al. [22] applied diffusion-based TGO growth and a 3D phase-field model to simulate interconnected 'mud-crack' formation, but these approaches do not capture delamination cracking within the TGO that ultimately drives spallation and coating failure. While these studies provide valuable insights, they largely address isolated mechanisms, leaving the combined effects of TGO growth, phase transformations, creep, thermal gradient, and interface morphology under realistic service conditions insufficiently understood.

The present work aims to address these limitations by developing a comprehensive modeling framework that incorporates multiple interacting phenomena. Stress distribution and evolution in EBCs are evaluated under realistic operating conditions by incorporating both thermal and mechanical loading during cyclic exposure. Critical phenomena such as dynamic TGO growth and phase transformations within the oxide layer are explicitly modeled based on established experimental evidence. A phase-field fracture approach is employed to capture crack initiation, propagation, and delamination. By combining these elements, the model is designed to reproduce the complex thermo-mechanical response of EBCs and provide predictive capability for analyzing failure mechanisms and estimating coating lifetime.

2. Literature Review

Increasing the turbine inlet temperature (TIT) is essential for boosting engine efficiency, as higher combustion temperatures allow for better gas expansion and improved thermodynamic performance. Figure 1(a) illustrates the historical and projected evolution of TIT and the temperature capability of hot zone structural materials from the 1960s through the 2030s [23], while figure 1(b) shows the nearly linear relationship between turbine core power and TIT between approximately 900°C and 1700°C [24], [25]. To meet future efficiency demands, TITs exceeding 1500°C are necessary. However, pushing these boundaries with current materials (super-alloys) comes at a cost. Lefebvre and Ballal [26] reported that NOx emissions increase sharply at combustion temperatures above 1600°C, highlighting a significant environmental concern. Rolls-Royce [27] observed that only about 40% of the air entering a turbine is used for combustion, with the remainder required for cooling. This not only introduces inefficiencies but also increases emissions from unburnt fuel, underscoring the urgent need for new materials that can withstand higher temperatures while reducing cooling requirements and emissions.

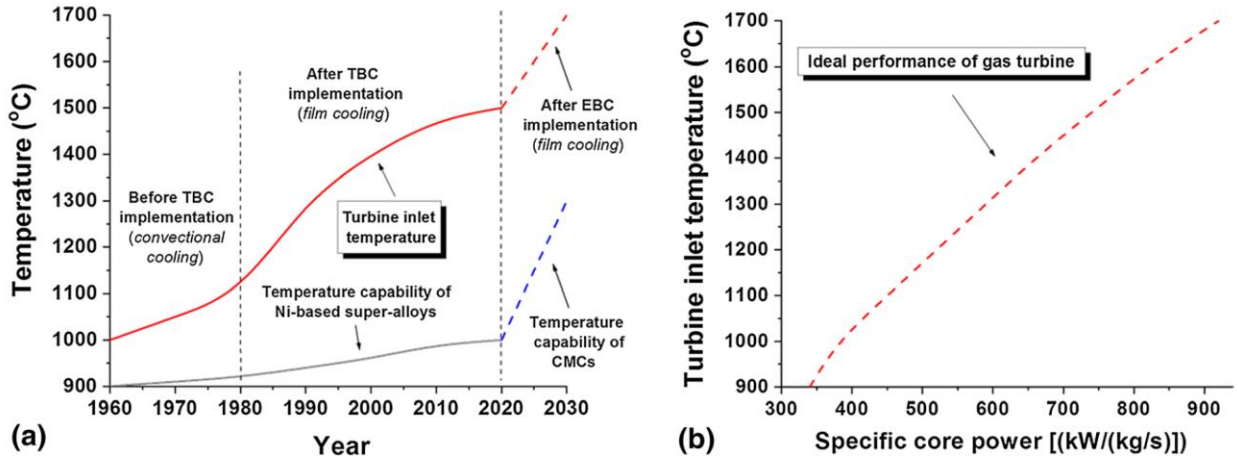

Figure 1: *(a) Evolution of combustion and structural part capability temperatures of gas turbines (b) Combustion temperature as a function of the specific core power of a gas turbine[23]*

In response to these growing demands, CMCs, particularly SiC/SiC composites (silicon carbide fibres in silicon carbide matrix), have emerged as promising alternatives due to their superior high-temperature strength, lower density, and enhanced thermal efficiency compared to conventional metallic alloys. In addition to their high temperature capabilities, CMCs can also help in lowering emissions. NOx forms through the reaction of N_2 and O_2 at high temperatures. Lefebvre and Ballal [26] reported that in conventional metallic-based combustion chambers, NOx emissions exceed acceptable levels (>15 ppmv) when combustion temperatures exceed 1600 °C. Therefore, increasing combustion temperatures beyond ~1500 °C to boost turbine performance is not a practical option due to the excessive NOx formation. Bhatia et al. [28] demonstrated that reducing the amount of cooling air required allows more air to be mixed with fuel during combustion, resulting in a 30% reduction in NOx emissions at full engine power and a 20% reduction in CO emissions at idle. The comparison of the NOx emissions produced in combustion chambers of gas turbine engines for different air/fuel mixing conditions is presented in Figure 2 [23].

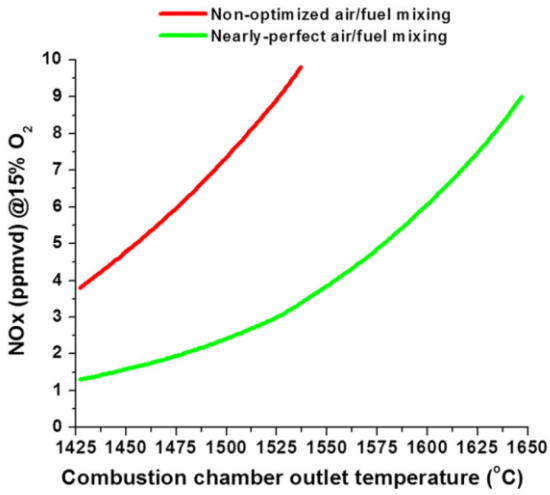

Figure 2: *Effects of the air/fuel fixing on NOx formation in gas turbines engines [23]*

Despite these advantages, the application of CMCs introduces new challenges, as these materials are highly susceptible to degradation from oxidation, water vapor, and environmental contaminants such as calcium-magnesium-alumino-silicates (CMAS). To ensure the reliable performance of CMCs in adverse operating environments, EBCs have been developed as advanced multilayer systems tailored to address these degradation mechanisms. EBCs provide not only thermal insulation but also critical protection against oxidation, corrosion, and CMAS infiltration—conditions that are beyond the protective capabilities of conventional TBCs.

By enabling CMC components to operate at temperatures exceeding 1350°C and under severe environmental conditions, EBCs play a pivotal role in maintaining structural integrity and long-term performance. Their development and implementation drive the advancement of next-generation turbine technologies with improved engine efficiency, reduced emissions, and enhanced power-to-weight ratios.

2.1. EBC Requirements and Challenges

An effective EBC system must possess several essential properties. Figure 3 illustrates the key challenges and requirements associated with EBCs, highlighting the phenomena triggered by high temperatures that the coating must withstand to maintain its protective role.

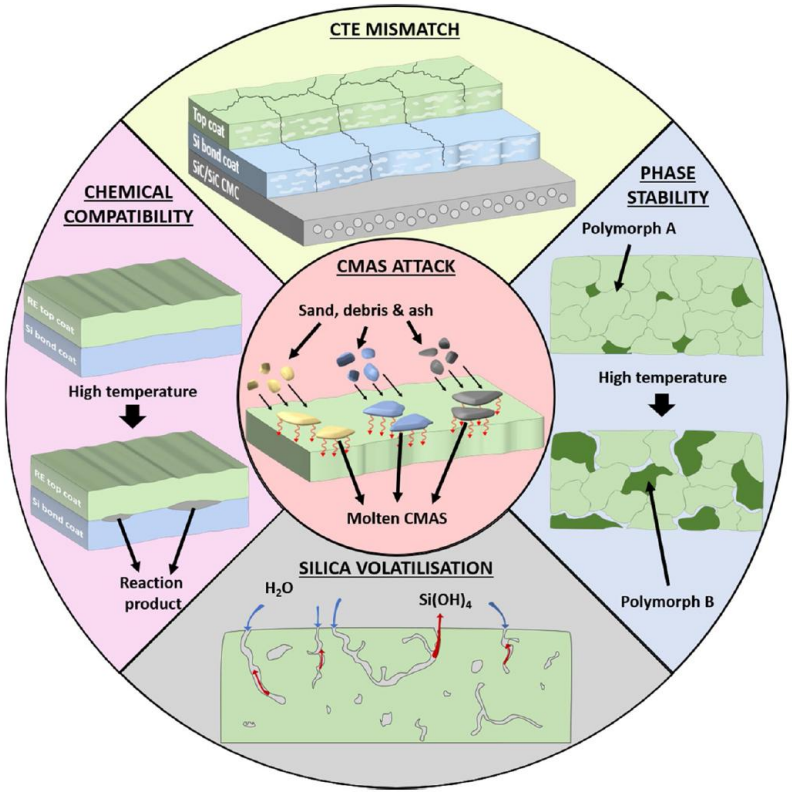

Figure 3: *Schematic of the main requirements of Environmental Barrier Coatings [29]*

In gas turbine environments, coating materials serve a critical role in shielding the substrate from water vapor–induced corrosion, which can otherwise lead to rapid degradation of the underlying bond coat and substrate. This protective barrier against water vapor is their primary function; however, for coatings to remain durable under cyclic thermal loading, their performance cannot rely on corrosion resistance alone. They must also possess a coefficient of thermal expansion (CTE) that is closely matched to that of the adjacent layers and the substrate, thereby minimizing

thermal stresses and preventing crack formation. The SiC substrate typically has a CTE of approximately 4.67 × 10^{-6} /°C, compared to commonly used EBC materials like $Yb_2Si_2O_7$ (~4 × 10^{-6} /°C), Yb_2SiO_5 (~7.5 × 10^{-6} /°C), and $3Al_2O_3 \cdot 2SiO$ (~5.3 × 10^{-6} /°C) [14], [15]. During service, heating and cooling cycles induce thermal expansion and contraction in the different layers of the EBC. When the CTE of the layers differ significantly, large thermal stresses develop, potentially leading to crack formation that can compromise the integrity of the EBC system over time.

Gatzen et al. [30] examined a range of oxides and silicates, categorizing them according to their recession rates and CTEs using data from Refs. [31], [32], shown in Figure 4. The analysis shows that oxides and silicates with the highest resistance to water vapor typically have CTEs exceeding those of SiC/SiC CMCs. Therefore, careful material selection is essential to minimize residual stresses arising from CTE mismatch during thermal cycling while still providing effective corrosion protection. Ytterbium disilicate ($Yb_2Si_2O_7$) appears to offer a favorable balance and has been widely investigated for use as an EBC.

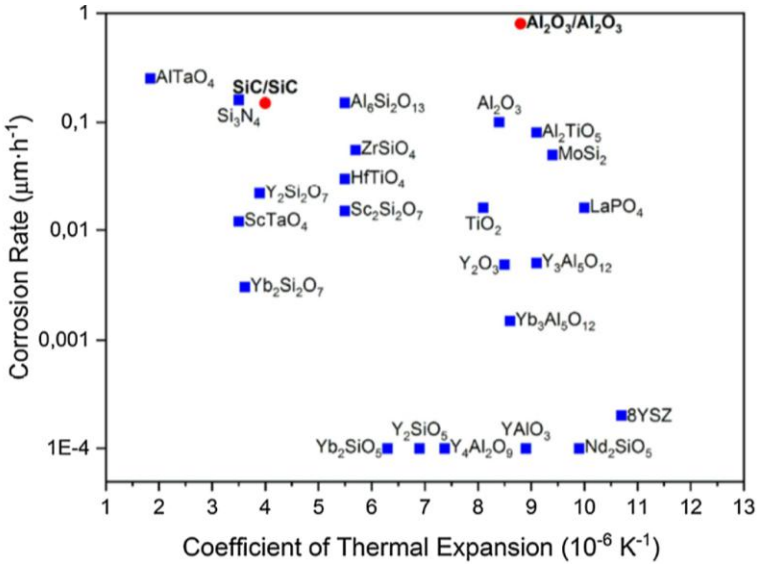

Figure 4: *Comparison of recession rates and coefficient of thermal expansion of various oxides and CMCs [30]*

Additionally, the coating should remain stable without undergoing any phase transformations at high temperatures. High temperatures can induce a phase transformation from one polymorph to another, leading to significant volume changes and residual stresses that may cause cracking and porosity. If transformations do occur, the CTE of the polymorphs involved should be similar, with minimal volume change. Additionally, silica volatilization poses a further challenge. The presence of steam at elevated temperatures leads to the formation of silica-containing gases, like $Si(OH)_4$, which contributes to material recession [33]. EBC should exhibit low silica activity under various conditions, including both dry and wet environments.

Furthermore, while materials may exhibit stability and compatibility at room temperature, they may become reactive at high temperatures, forming unwanted by-products after prolonged exposure. This highlights the necessity of chemical compatibility between the layers to avoid the formation of undesirable reaction products at the interfaces, which could undermine the structural integrity of the EBC. Lastly, the accumulation of debris and impurities can lead to the formation of molten deposits of corrosive species, known as CMAS at temperatures above ~1230 ^{o}C. When CMAS melts, they bond to hot section components, leading to harmful chemical reactions with EBCs that can induce aging stress. Moreover, the molten CMAS can penetrate porous EBCs, raising their modulus and consequently increasing the stress within the EBC [24]. Therefore, the melting temperature of CMAS determines the upper limit of the combustion temperature of gas turbines.

2.2. Structure of EBC Systems

A single material cannot meet all the requirements of the EBC, and as a result, modern EBCs have evolved into multilayer coatings. A schematic representation of a typical multi-layered EBC

system is presented in Figure 5, highlighting the topcoat, intermediate layer, TGO, bond coat, and SiC/SiC substrate, with thermal cycling applied at the surface.

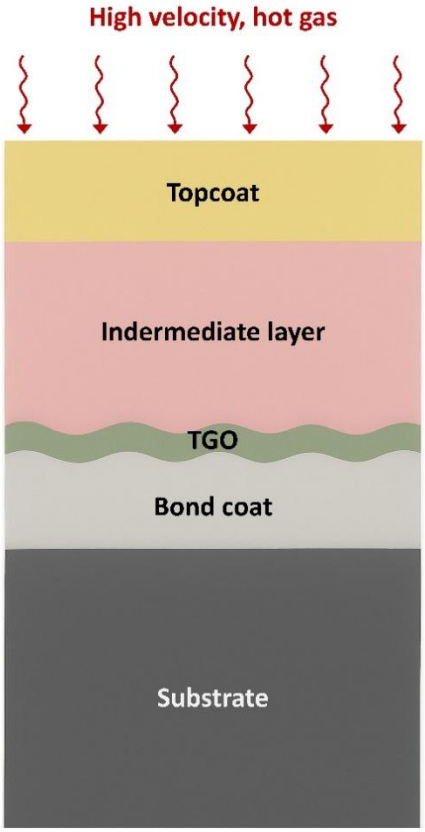

Figure 5: *Schematic representation of a typical multilayered EBC system*

Each layer serves specific functions aimed at providing comprehensive protection to the underlying CMC substrate. The coating layers are usually ~100-200 µm in thickness. The standard structure of an EBC system includes the following layers:

1. **Topcoat:** The topcoat is the outermost layer of the EBC system, designed to provide direct protection against environmental degradation from high-temperature steam and molten CMAS. Rare-earth silicates, such as $Yb_2Si_2O_7$, are often used as topcoat materials due to their low oxygen permeability and resistance to chemical reactions with CMAS. The topcoat serves as the first line of defense, shielding the underlying layers and the CMC

from high-temperature corrosion, moisture, and foreign particle ingestion during turbine operation.

2. **Bond Coat:** The bond coat is applied directly onto the CMC substrate and serves as the adhesive interface between the topcoat and the underlying substrate. Silicon is frequently used as a bond coat due to its compatible CTE with SiC-based CMCs and its ability to form a protective silica (SiO_2) layer upon oxidation. This silica layer contributes to enhanced oxidation resistance and helps maintain the integrity of the bond between the coating and the substrate during thermal cycling.
3. **Thermally Grown Oxide Layer:** While the oxide layer may not be directly deposited, it forms naturally above the bond coat during high-temperature operation due to the oxidation of the bond coat. Typically composed of SiO_2, the TGO plays a dual role: providing additional oxidation protection to the substrate and inducing thermal stresses during its growth. Excessive TGO growth can lead to cracking and spallation of the coating, making it a critical factor in the long-term reliability of EBC systems.
4. **Intermediate Layers:** In some EBC designs, one or more intermediate layers can be added to address specific challenges such as chemical compatibility, CTE transitions, water vapor stability, and oxidation and CMAS resistance [24]. These intermediate layers particularly help to alleviate thermal expansion mismatches between the coating layers and the substrate, thereby reducing the risk of thermal stress-induced failure. Materials such as ytterbium monosilicate (Yb_2SiO_5) and mullite are often employed due to their favorable thermomechanical properties. In addition to providing a graded transition in thermal expansion, they may offer additional resistance to oxygen and moisture ingress.

2.3. EBC Failure Modes

The degradation of EBCs can generally be classified into two categories: environmental/chemical and thermal/thermo-mechanical [24]. Environmental and chemical degradation includes water vapor–induced recession, steam oxidation, and damage from CMAS deposits. Thermal and thermo-mechanical degradation, on the other hand, arises from thermal mismatch stresses, cyclic thermo-mechanical loading, particle erosion, and foreign object damage (FOD). EBC degradation and failure modes have been schematically presented in figure 6 [34].

EBC failure is most often driven by the development of stresses, regardless of whether the underlying degradation mechanism is environmental, chemical, thermal, or thermo-mechanical in nature. [24] The total stress in an EBC (σ_{EBC}) on a CMC substrate can be expressed as:

$$\sigma_{EBC} = \sigma_t + \sigma_a + \sigma_g \tag{1}$$

where σ_t is the thermal mismatch stress, σ_a is the aging stress, and σ_g is the growth stress [35].

The thermal mismatch stress is given by:

$$\sigma_t = \frac{(\alpha_{EBC} - \alpha_{CMC})E_{EBC}\Delta T}{1 - \mu_{EBC}} \tag{2}$$

where α_{EBC} and α_{CMC} represent the CTE of the EBC and CMC substrate respectively, E_{EBC} is the Young's modulus, and μ_{EBC} is the Poisson's ratio of the coating [34].

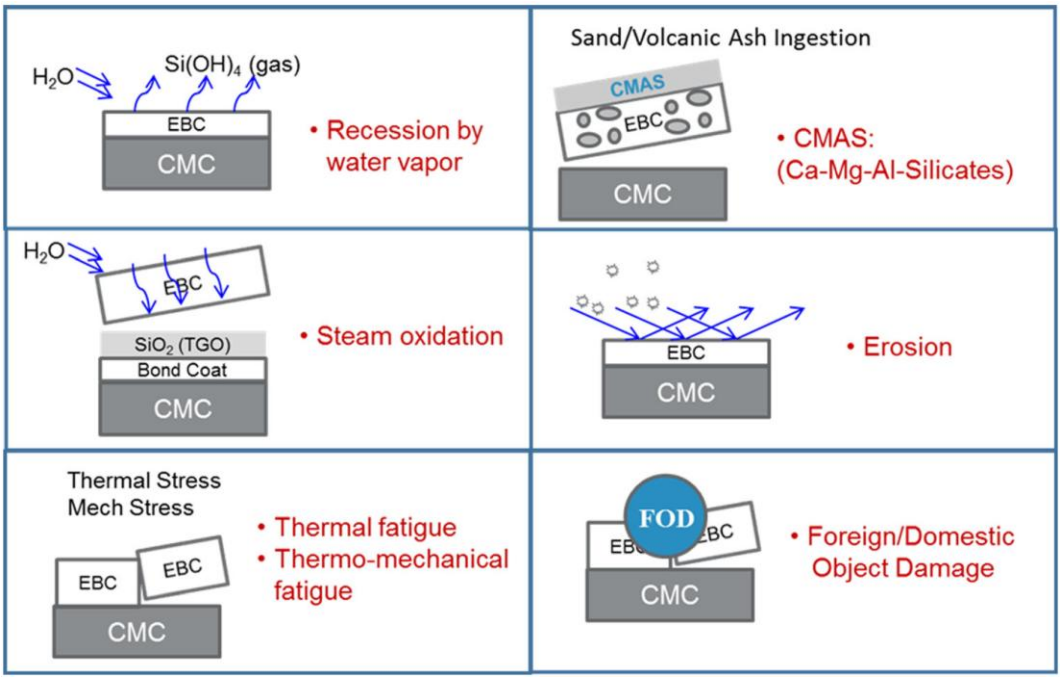

Figure 6: *Schematic illustrating EBC failure modes* [34]

Aging stress arises from time-dependent changes in the physical, mechanical, and chemical properties of the EBC during thermal exposure, including oxidation, chemical reactions, phase transformations, and sintering. The growth stress, by contrast, originates during coating deposition. In addition, other stresses—such as thermal shock stresses induced by steep temperature gradients—can further contribute to EBC degradation but are not captured in Eq. (1).

Among these processes, silicon recession by water vapor in the topcoat and subsequent steam oxidation of the Si bond coat are particularly critical. Recession enables oxidizer ingress, while oxidation promotes the growth of a TGO. The buildup of residual stresses during TGO growth frequently results in spallation of the coating, making this coupled degradation particularly detrimental and central to the present study.

2.3.1. Steam Degradation and Silica Volatilization:

Although SiC/SiC CMCs are considered highly promising material for advancing gas turbine hot section technology, one significant drawback is the volatilization of Si caused by water vapor from combustion reactions, leading to rapid surface erosion. In oxygen-rich environments, SiC forms a thin protective SiO_2 scale:

$$SiC\ (s) + 2O_2\ (g) \rightarrow SiO_2\ (s) + CO_2\ (g) \quad (3)$$

The silica layer (SiO_2) formed on the SiC surface acts as a protective layer initially because it slows down further oxidation. Over time, the silica layer becomes susceptible to reactions with environmental water vapor. In environments containing high water vapor (90% H_2O and 10% O_2), silica (SiO_2) reacts with water vapor to form volatile silicon hydroxide species ($Si(OH)_4(g)$):

$$SiO_2\ (s) + 2H_2O\ (g) \rightarrow Si(OH)_4\ (g) \quad (4)$$

This volatilization process gradually erodes the SiO_2 layer, which exposes the underlying SiC substrate to further oxidation and degradation, leading to continuous material loss and eventual structural failure [36]. EBCs mitigate this degradation by providing a protective barrier.

Water vapor acts as the main oxidizing agent for SiC in environments where both water vapor and oxygen are present. The rate at which H_2O diffuses through SiO_2 is about 100 times slower than O_2, however, its solubility in SiO_2 is approximately 1000 times higher than that of O_2. Since permeability is the product of diffusivity and solubility, the permeability of H_2O in SiO_2 is ~10 times greater than that of O_2 [34].

The silica volatility model developed by Opila et al.[37], quantitatively describes the volatility of silica in steam environments:

$$J(\mathrm{Si(OH)_4}) = a(\mathrm{SiO_2}) \cdot v^{1/2} \cdot P\ (\mathrm{H_2O})^2\ P_{\mathrm{total}}{}^{1/2} \quad (5)$$

Where, $J(\mathrm{Si(OH)_4})$ is the SiO_2 volatility, $a(\mathrm{SiO_2})$ is the silica activity of EBC, v is the gas velocity, $P\ (\mathrm{H_2O})$ is the water vapor pressure, and P_{total} is the total pressure.

Materials with lower silica activity corresponds to lower volatility and therefore, are desirable in a high temperature steam environment such as gas turbines. Based on the model described in Eq. 5 and thermogravimetric analysis, the volatility of various rare earth silicates, mullite, and BSAS were compared, where rare earth monosilicates (e.g., Yb_2SiO_5 and Y_2SiO_5) demonstrated the least silica volatility, followed by rare earth disilicates (e.g., $Yb_2Si_2O_7$, $Y_2Si_2O_7$), BSAS, and mullite. [38]. This is attributed to the significantly lower silica activity of the rare earth monosilicates, which is about two orders of magnitude lower than that of the disilicates [39], [40]. Based on findings, the volatility ranking among silicates is as follows: mullite > BSAS > rare earth disilicates > rare earth monosilicates [24].

The volatilization of rare earth silicates in water vapor follows these reactions [33]:

$$\mathrm{RE_2Si_2O_7} + 2\mathrm{H_2O}(g) \rightleftharpoons \mathrm{RE_2SiO_5} + \mathrm{Si(OH)_4}\ (g) \quad (6)$$

$$\mathrm{RE_2SiO_5} + 2\mathrm{H_2O}\ (g) \rightleftharpoons \mathrm{RE_2O_3} + \mathrm{Si(OH)_4}\ (g) \quad (7)$$

Although RE monosilicates offer superior resistance to water vapor recession due to their low silica activities compared to its disilicate counterpart [38], [39], [40], they have significantly higher CTEs than CMCs, which increase residual stress in the coatings. RE monosiliate coatings have

exhibited issues with porosity and vertical cracking, also known as mudcracks, under steam cycling conditions [15]. On the other hand, RE disilicate offer low oxygen permeability and CTE compatibility. However, when exposed to steam at elevated temperatures, RE disilicates undergo transformation to form RE monosilicate by following the reaction shown in Eq 6.

Ytterbium silicates, specifically Yb_2SiO_5 and $Yb_2Si_2O_7$, are more popular choices for EBCs due to their lower silica volatility and better CTE match with SiC. In the case of $Yb_2Si_2O_7$/Si bi-layer EBC system, the transformation from $Yb_2Si_2O_7$ to Yb_2SiO_5 occurs following the reaction shown below:

$$2Yb_2Si_2O_7(s) + 2H_2O(g) \rightarrow Yb_2SiO_5(s) + Si(OH)_4(g) \quad (8)$$

After 2000 thermal cycles with a holding period of 60 minutes per cycle, the Yb_2SiO_5 corrosion layer was reported to be in the range of 5 to 15 μm [14]. The growth followed a parabolic law [41], indicating a diffusion-controlled process and is expressed as:

$$\delta^2 = k_p.t \quad (9)$$

where δ is the thickness of the corrosion layer, t is the steam cyclic time (in seconds), and k_p is the corrosion kinetic constant ($2.16 \times 10\ 11\ mm^2 \cdot s^{-1}$) [21].

The volatilization of $Si(OH)_4$ from the surface of $Yb_2Si_2O_7$ surface and its subsequent transformation to Yb_2SiO_5 following the reaction shown in Eq. 8 and illustrated in figure 7 is accompanied by a volume reduction of 26% [14] and ~20% porosity [14], [41]. The increased porosity in Yb_2SiO_5 can be attributed to the formation of creep-induced voids at high temperature

which partially relieves the shrinkage stress associated with $Yb_2Si_2O_7 \rightarrow Yb_2SiO_5$ transformation [14].

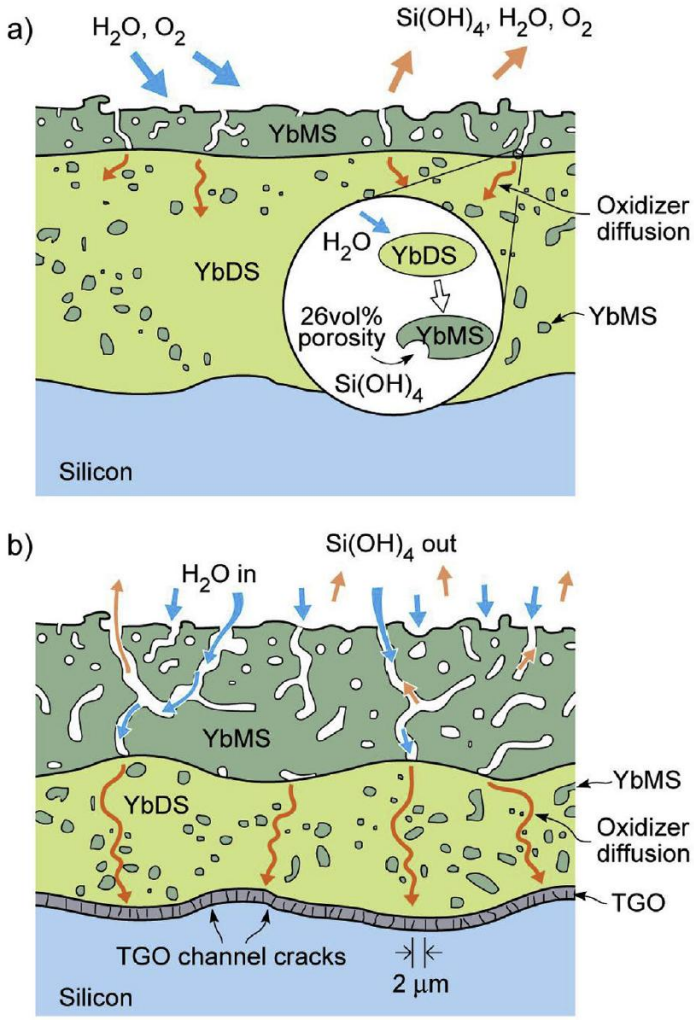

Figure 7: *Schematic representation of the volatilisation of silica from the initial $Yb_2Si_2O_7$ and formation of Yb_2SiO_5 (a) shows the initial stage of the process, while (b) shows the late stages [14]*

Yb_2SiO_5 develops tensile stresses, whereas the $Yb_2Si_2O_7$ topcoat remains in a state of compressive stress [14], [21]. This stress distribution arises from the combined effects of residual shrinkage strain and the mismatch in CTE between Yb_2SiO_5 and the underlying substrate. The CTE of Yb_2SiO_5 ($7.5 \times 1\ 0^{-6}$ /°C) is larger than that of the original $Yb_2Si_2O_7$ ($\sim 4 \times 1\ 0^{-6}$ /°C) and SiC (4.67×10^{-6} /°C), which intensifies the thermal mismatch and generates tensile stress in the

Yb_2SiO_5 corrosion layer [14], [15]. SEM images in figure 8 [14] show that after 2000 cycles, the surface layer becomes highly porous, and due to the effect of tensile stress (σ_{11}), vertical cracks, also known as 'mud cracks' with large opening displacements appear on the surface of the transformed Yb_2SiO_5 layer. These cracks provide direct pathways for oxidizers to penetrate to the silicon bond coat, thereby accelerating TGO formation and further compromising the integrity of the coating system. Delamination cracks that led to spallation of the modified surface region can be observed in figure 8(b).

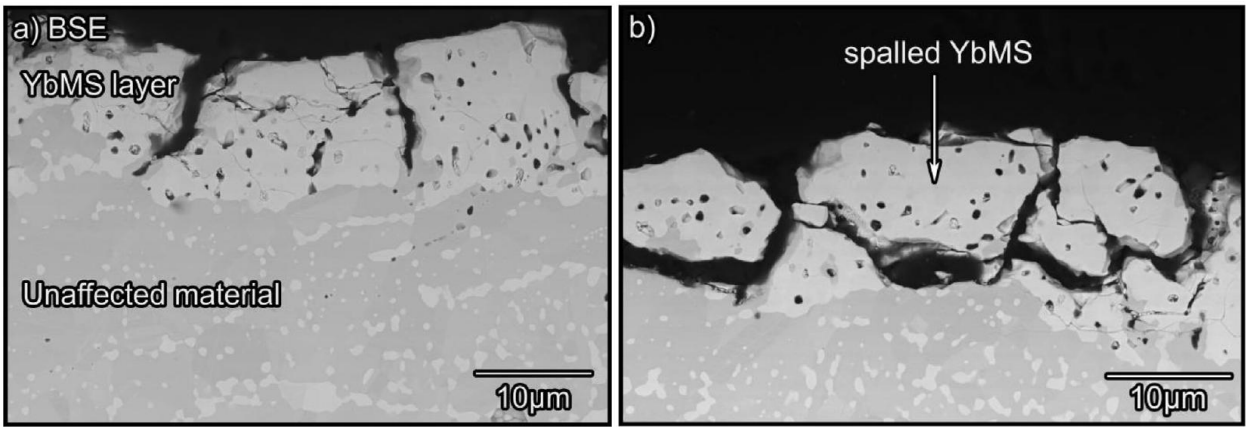

***Figure 8**: BSE micrograph of a surface volatilized region of the topcoat. (b) Spalled region of surface volatilized layer after 2000 steam cycles at 1316°C [14]*

2.3.2. Bond Coat Oxidation

In water vapor environment, the water vapor permeates through the $Yb_2Si_2O_7$ topcoat and reacts with the Si bond coat, forming a layer of SiO_2 scale, referred to as TGO, at the bond coat/ topcoat interface. The TGO growth can be modeled as function of time. While a few studies such as the work by Richards et al. [14] have reported a perfectly linear growth of TGO, the majority of investigations indicate that TGO growth follows nonlinear kinetics, most commonly characterized by a parabolic behavior [34]. Nevertheless, perfectly parabolic growth is rarely observed in

practice, as the oxidation rate is highly temperature-dependent and tends to accelerate at elevated temperatures, leading to deviations from ideal parabolic kinetics.

Richards et al. [14] identified α-cristobalite as the form of SiO_2 TGO through Raman analysis during a cyclic oxidation study of plasma-sprayed Si/$Yb_2Si_2O_7$ EBC on α-SiC Hexoloy™ at 1316°C in a water vapor environment (90% H_2O + 10% O_2). The oxide initially forms as β-cristobalite at 1316 °C and transforms to α-cristobalite upon cooling near 200°C, accompanied by ~5% volume shrinkage [14], [34], [42], [43]. Large residual stresses (~4 GPa) were reported in the TGO [14], [15]. This can be attributed to several factors. During high temperature service period, the oxidation of Si bond coat induces a ~2.2-fold volume expansion [14], generating significant growth stress. During the cooling cycle following β to α cristobalite transformation, the associated volume shrinkage combined with CTE mismatch between the α cristobalite and EBC materials produce significant tensile stress within the TGO.

The residual tensile stresses in the TGO accumulate strain energy, which serves as the primary driving force for oxidation-induced failure [34], [44]. Once the TGO thickness exceeds ~1.5 μm, the stored energy surpasses the critical threshold for vertical crack propagation, leading to closely spaced ‘mud cracks’ that fully penetrate the TGO [14], [45]. These vertical cracks often bifurcate, promoting interfacial delamination, which is one of the most frequently observed EBC failure modes [46]. In the $Yb_2Si_2O_7$/Si system, the strain energy release rate (G) for delamination was measured to be below 20 N/m for cristobalite scales up to 5 μm thick in fully dense coatings, and decreased by ~50% in porous coatings produced by atmospheric plasma spray (APS) [14]. These findings support a strain energy–driven mechanism where TGO cracking and subsequent delamination govern EBC failure.

Vertical “mud-cracks” in the TGO often branch within the oxide to form complex three-dimensional crack networks [22], [45]. Such branching is significant because interconnected cracks provide short-circuit diffusion pathways, accelerating TGO growth during thermal cycling. The presence of a topcoat further constrains stress relaxation in the TGO, leading to reduced crack spacing, consistent with experimental observations by Bakan and Vaßen [22], [47]. While most branching occurs within the TGO, cracks can also extend into adjacent layers, where they may either deflect along interfaces or penetrate into the bulk, depending on the fracture mode and interfacial toughness [48]. These interfacial cracks are especially detrimental, as they promote delamination and significantly reduce EBC lifetime.

To improve the lifespan of EBCs, reducing the growth rate of the TGO is critical. Lee et al. [34] demonstrated that modifying a baseline Si/$Yb_2Si_2O_7$ EBC with oxide additives like Al_2O_3 and TiO_2 reduced TGO growth by limiting oxidant permeability through both the topcoat and the TGO. TGO thickness for the baseline, Group I (Al_2O_3-based modifiers), and Group II (TiO_2-based modifiers) EBCs after 100, 500, and 1000 hours of steam cycling is reported in Table 1. After 1000 hours of thermal cycling in 90% H_2O + 10% O_2 between 1316 °C and 110 °C, the baseline EBC formed a ~13 μm thick TGO with extensive cracking, likely associated with cristobalite formation. In contrast, Al_2O_3-based modifiers reduced TGO thickness to ~1.7–1.9 μm (an 87% reduction) and exhibited no cracking, suggesting the formation of a more stable, amorphous oxide.

Table 1 *TGO thickness (μm) of baseline and modified EBCs in 90% H_2O + 10% O_2 at 1316°C in thermal cycling [34]*

EBC group	EBC ID	Environment	100 h		500 h		1000 h	
			AVG[a]	SD[b]	AVG[a]	SD[b]	AVG[a]	SD[b]
Baseline	B	Air	0.8	0.2	2.0	0.3	3.3	0.5
		Steam	4.7	0.8	10.6	2.7	13.2	3.9
I	6A	Steam	0.2	0.1	1.3	1.0	1.9	0.8
	M2Y		1.0	0.4	1.4	0.2	1.7	0.5
	3M		1.4	0.7	1.4	1.2	2.5	2.1
	2Y		1.5	0.9	3.7	1.1	3.7	1.6
	M5Y		0.8	0.3	1.3	0.3	2.4	0.6
II	M		4.0	1.0	11.6	1.7	16.3	5.4
	AT		3.4	0.7	7.4	2.5	10.0	2.6
	MT		4.8	1.3	10.8	1.3	10.8	0.9

Figure 9 compares the cross-sections of Si/$Yb_2Si_2O_7$ and Si/$Yb_2Si_2O_7$ + 4.66 wt.% YAG + 1.39 wt.% mullite EBCs after 1000 one-hour cycles at 1316 °C [34]. The addition of YAG and mullite significantly reduced TGO growth rates, limiting crack formations and extending the EBC lifespan.

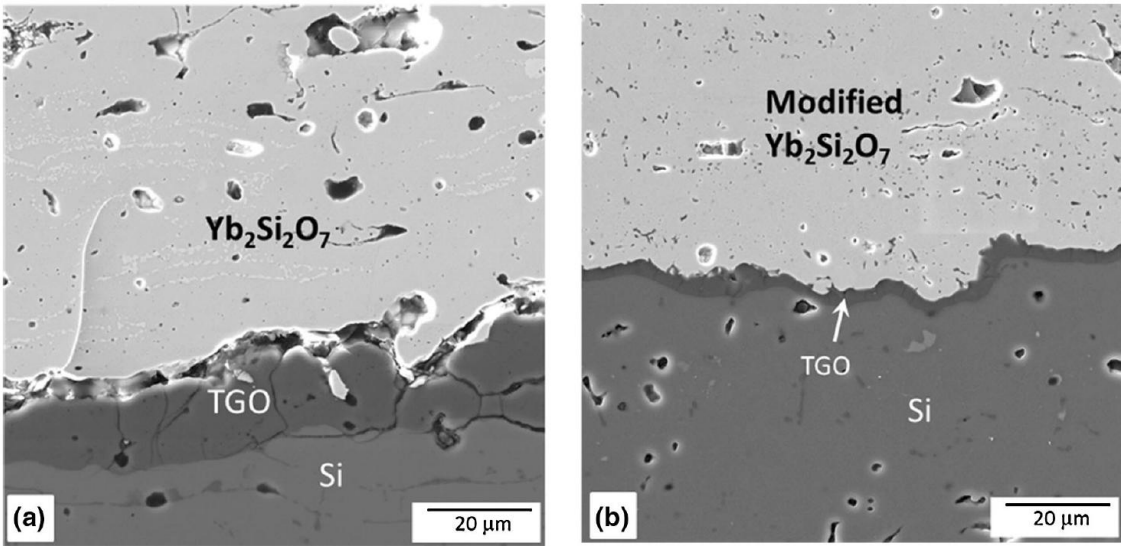

Figure 9 *Cross section of (a) silicon/Yb2Si2O7 and (b) silicon/Yb2Si2O7 + 4.66 wt.% YAG + 1.39 wt.% mullite EBCs on CMC after 1000 1-hour cycles at T = 1316 °C [34]*

If we assume that the parabolic oxidation rate constants remain consistent throughout the lifespan of EBCs, and that the critical TGO thickness at which EBCs fail due to spallation is identical for all EBCs, the lifespan for EBCs can be estimated using the following equations:

$$x_{cr}{}^2 = k.t_{life} \tag{10}$$

$$t_{life} = x_{cr}{}^2 / k \tag{11}$$

where, x_{cr} is the critical TGO thickness at failure (μm), k is the oxidation rate constant (μm²/h), and t_{life} is the EBC lifespan, or the time to failure (hours). Therefore, slower TGO growth rates correspond to increased EBC lifetime.

2.3.2.1. Interface Undulations

Interfaces between EBC layers are typically irregular and undulated, which plays a critical role in coating durability. Such non-uniform geometries break translational symmetry and act as preferential sites for stress concentration and crack initiation. Unlike flat interfaces where stresses are expected to be uniform throughout the material, undulations generate steep stress gradients across peaks, valleys, and transitional regions due to differential strain during thermal cycling.

Using the finite element method, Cheng et al. [23] demonstrated that undulated interfaces not only intensify stress localization but also influence TGO morphology over time due to diffusion-mediated amplification of interface roughness. When oxidant permeability through the topcoat (Pa) is significantly lower than that through the TGO (Pb), i.e., Pa:Pb = 1:2, oxidation is governed by diffusion through the topcoat and oxidant flux is concentrated at interface peaks due to shorter diffusion paths, accelerating local TGO growth at the peaks. This leads to a non-uniform oxide profile and progressive amplification of the initial interface roughness. This is consistent with

experimental observations by Ridley et al. [49], who observed highly nonuniform TGO morphology in EBC systems fabricated with intentionally roughened interfaces. Conversely, when the topcoat is highly permeable, oxidation occurs more uniformly, which preserves the original interfacial profile.

The growth of TGO along rough interfaces also generates substantial residual stresses. Cheng et al. [22] reported that stresses are concentrated near peaks and their magnitudes are strongly dependent on the amplitude and wavelength of the undulations: larger amplitudes intensify localization whereas longer wavelengths reduce stress concentrations. Amplified roughness further dictates the pattern, spacing, and connectivity of crack networks. Cracks initiated at rough interfaces may bifurcate and coalesce into delamination fronts or propagate upward into the topcoat and downward into the bond coat depending on the local stress distribution and material toughness. These results are validated by experimental observations of Bakan and Vaßen [50] shown in figure 10, which demonstrate that the surface finish of the Si layer affects TGO thickness, morphology and crack density. The polished Si surface produces a thinner, more uniform, and less-cracked TGO compared to unpolished Si.

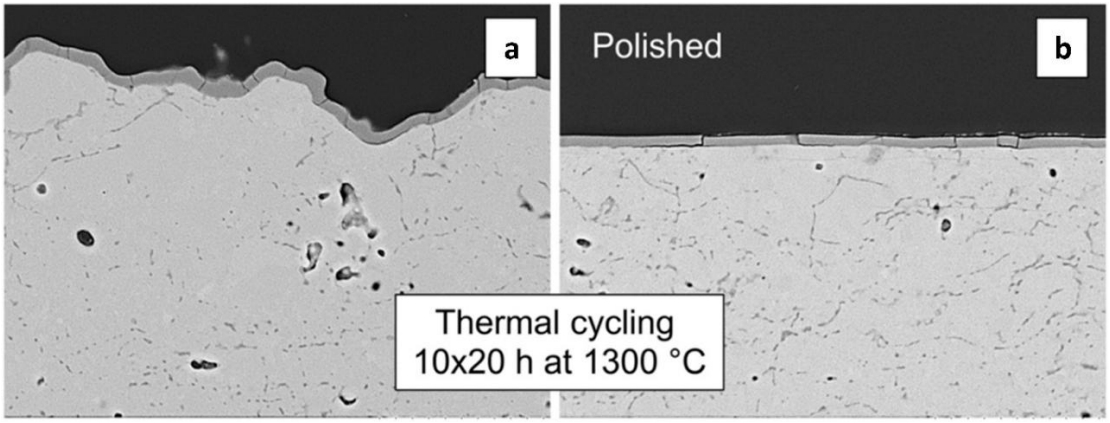

Figure 10: *Cross-section SEM micrographs of APS Si coatings after thermal cycling oxidation (200 h at 1300 ◦C, air) tested in (a) as-sprayed state and (b) and after polishing[50]*

In the present study, the topcoat/bond coat interface is represented by a simplified sinusoidal profile with an amplitude of 10 μm and a wavelength of 200 μm to capture the effects of interfacial undulations. The influence of oxidation diffusion paths on TGO morphology is not explicitly considered, and the oxide thickness is assumed to grow uniformly across the interface.

3. Research Objectives

Recent studies on thermal and environmental barrier coatings have examined residual stress formation [7], [9], [10], [13], the influence of interfacial roughness and coating thickness on stress localization and crack initiation [11], [19], [20], and water-vapor-induced phase transformations that accelerate cracking and delamination [21]. More advanced approaches, such as diffusion-based TGO growth modeling and 3D phase-field simulations [22], have captured oxide evolution and surface crack formation, but they generally address isolated mechanisms rather than the combined effects encountered under realistic service conditions. A fully integrated modeling framework is therefore needed to reproduce and predict the complex fracture behavior and failure mechanisms observed experimentally in EBC systems.

The objectives of this research are to:

1. Develop a comprehensive finite element model that simulates realistic in-service conditions of gas turbines by incorporating the effects of thermo-mechanical loading, heat transfer, creep, phase transformations, and oxidation kinetics.
2. Evaluate stress distribution and evolution in EBC systems during thermal cycling, with emphasis on regions susceptible to damage.
3. Predict fracture initiation and propagation using phase-field and fracture mechanics approaches and propose a failure mechanism leading to coating spallation.

4. Perform parametric studies to examine the effects of oxidation kinetics/ TGO thickness, and interface morphology on crack evolution and overall EBC durability.
5. Validate model predictions against experimental findings reported in the literature to ensure accuracy and reliability.

By addressing these objectives, this study aims to establish a predictive modeling framework that captures the coupled multi-physics processes driving EBC degradation, providing deeper insight into failure mechanisms and guiding the design of more durable coatings for next-generation turbine applications.

4. Material Models and Modelling Methodology

4.1. SiO_2 TGO Growth Model and $Yb_2Si_2O_7$ Transformation to Yb_2SiO_5

The growth of SiO_2 TGO plays a crucial role in stress evolution within the EBC, as well as in the associated nucleation and propagation of cracks. In this paper, experimentally measured data on SiO_2 TGO growth are used to describe the kinetics of TGO growth. The derived TGO growth model is then incorporated into the COMSOL multi-physics package to simulate stress distribution and evolution under thermal cycles. The model also incorporates a corrosion layer, Yb_2SiO_5, formed on top of the $Yb_2Si_2O_7$ topcoat through its reaction with water vapor, resulting in transformation into Yb_2SiO_5 described in Eq. (8).

The corrosion and TGO layers undergo a time-dependent growth. The thickness of these layers as a function of time is shown in Figures 11(a) and (b). In this study, the thickness of the TGO and corrosion layer is assumed to grow only at the dwell temperature of 1316 °C, while it remains unchanged during the heating and cooling processes. The TGO growth is described by the parabolic oxidation law [34]Click or tap here to enter text., given by:

$$\mathbf{x_{TGO}(n)} = \sqrt{(\boldsymbol{a_c}.\mathbf{k_o}).\mathbf{n}} \tag{12}$$

Where, $x_{TGO}(n)$ is the thickness of the TGO layer after n cycles, a_c is the acceleration factor, and k_0 = 0.18 µm/cycle is the oxidation rate constant [34]. To evaluate a long-term degradation, an acceleration factor, a_c, equal to 100 was introduced into all time-dependent equations, including the growth equations, effectively simulating 1000 hours of steam exposure in 10 simulation cycles. This approach allows for a more comprehensive evaluation of stress evolution over extended operational periods while maintaining computational efficiency. This growth is captured in the FEM model using a deformed geometry functionality in COMSOL that allows the shape of the computational domain to change over time.

For the Yb_2SiO_5 layer, the growth is governed by a similar time-dependent equation [21], where the thickness is described as:

$$\mathbf{x_c(t)} = \sqrt{(\boldsymbol{a_c}.\mathbf{k_c}).\mathbf{t}} \tag{13}$$

where x_c(t) is the thickness of the Yb_2SiO_5 corrosion layer at time t, a_c is the acceleration factor as in Eq. (12), and k_c is the corrosion rate constant, which is 2.16×10−5µm/sec [21].

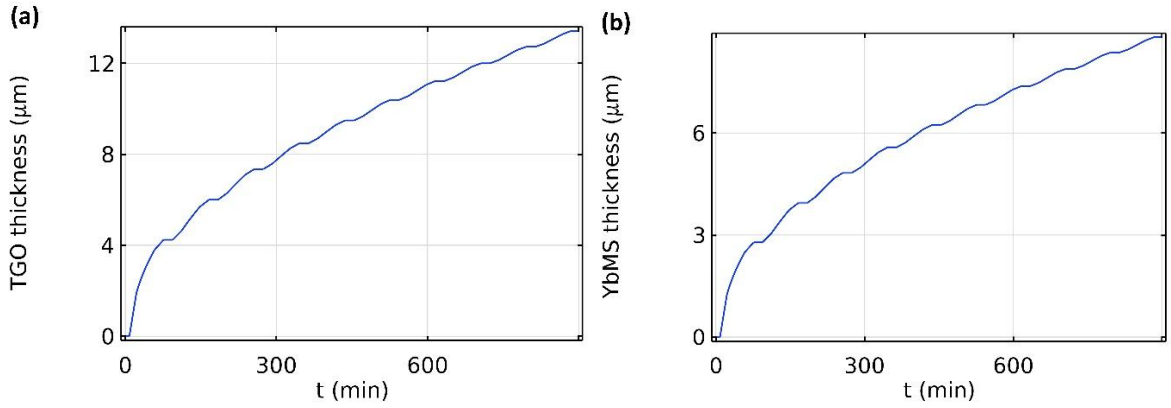

Figure 11: Thickness of (a) SiO_2 TGO, and (b) Yb_2SiO_5 corrosion layer as a function of time.

The model incorporates the β-α phase transformation in the TGO, which occurs between 220°C and 270°C [45] to account for changes in material properties and the associated shrinkage during cooling. This transformation leads to a volumetric shrinkage of approximately 5%, [14], [43], which corresponds to a linear shrinkage strain of about 1.67% in each of the *x*, *y*, and *z* directions. The change in material properties is defined as a function of temperature within the transformation range. The evolution of the α and β cristobalite phase fractions between 110°C and 1316°C is shown in Figure 12. Additionally, the oxidation of the Si bond coat leads to the formation of SiO_2, causing ~100% volume expansion [15] which translates to a large linear strain of approximately 26% in each directionClick or tap here to enter text..

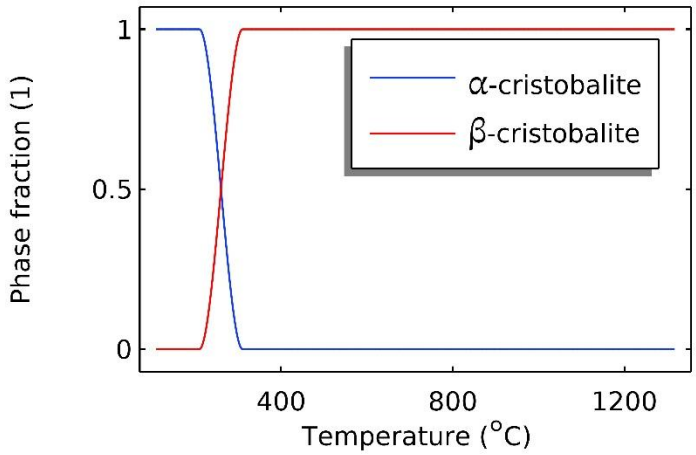

Figure 12: *Phase fraction of α and β cristobalite between 110 °C and 1316 °C.*

Similarly, a ~26% volume shrinkage, along with a 20% increase in porosity, is reported [14] during the transformation of $Yb_2Si_2O_7$ to Yb_2SiO_5 due to its reaction with water vapor described in Eq. 8. However, most of the volume shrinkage strain generated by $Yb_2Si_2O_7$ corrosion was relieved through the pores in the Yb_2SiO_5 layer. Consequently, only a small residual shrinkage strain ~5% was assigned to the corrosion zone [21].

4.2. Creep Models

During the high-temperature service period, the material's creep properties can largely determine the deformation behavior and, consequently, govern the strain-stress evolution. In the present paper, the creep models from the literature for Yb_2SiO_5, $Yb_2Si_2O_7$, SiO_2 TGO, Si bond coat, and SiC substrate are used and incorporated into the COMSOL simulation package. Under the thermal cycling at high temperatures, the topcoat, TGO, and bond coat can constantly reshape their microstructure and relax the residual stress [51]. The experiments have demonstrated that the creep behavior is formulated with the Norton power law, and the model has been widely applied in multiple high-temperature coating failure studies with FEM analysis [7], [52], [53], [54], [55], [56]. The governing equation for creep behavior is described as Eq. (14):

$$\dot{\epsilon}_{cr} = \frac{\delta\epsilon}{\delta t} = A_{nor}\left(\frac{\sigma}{\sigma_{ref}}\right)^{n} exp\left[\frac{Q}{R}\left(\frac{1}{T} - \frac{1}{T_{ref}}\right)\right] \quad (14)$$

where $\dot{\varepsilon}_{cr}$ is the creep strain rate, A_{nor} is the creep rate coefficient, σ is the residual stress, n is the stress exponent, Q is the activation energy, T is the system temperature, and T_{ref} is the reference temperature. Creep deformations of $Yb_2Si_2O_7$, Yb_2SiO_5, Si bond coat, SiO_2 TGO, and SiC substrate are considered in the modelling, with their respective model properties listed in Table 2. Since creep model parameters for the Yb_2SiO_5 are not available in the literature, the creep model parameters for $Yb_2Si_2O_7$ were adopted for Yb_2SiO_5. Due to the lack of data, this assumption is based on both materials being ytterbium silicates with similar chemical composition and crystal structure, and their high-temperature deformation is expected to be governed by similar diffusion-controlled mechanisms. The developed computational model can be readily updated in the future as more accurate material properties become available.

The material properties of the layers are assigned based on available experimental data. The Young's modulus for the $Yb_2Si_2O_7$ topcoat and the Si bond coat is assumed to be half of the bulk

material, considering the high porosity of APS coatings [14], [15], [57]. The modulus of Yb_2SiO_5 corrosion layer is further reduced from 86 GPa [12] to 63 GPa [21] to account for the increased porosity (~20%) in the layer during transformation shown in Eq. 8. The temperature dependence of thermal conductivity (k) and specific heat (C) is considered for Yb_2SiO_5 and $Yb_2Si_2O_7$, while other properties are assumed to remain constant over the temperature range. The material properties of the EBC materials used in the model are shown in Tables 2–5.

Table 2: *Creep Properties of EBC Materials [16], [58], [59], [60] .*

	A_{nor} (1/s)	σ_{ref} (MPa)	n	T_{ref} (°C)	Q (kJ/mol)
Yb_2SiO_5	1.23e^{-8}	15.8	1	900	135
$Yb_2Si_2O_7$	1.23e^{-8}	15.8	1	900	135
SiO_2	1.00e-4	84	4	1050	225
Si	1.67e-06	6.9	3.5	1100	39
SiC	7.50e-10	147	5	1575	695

Table 3: *Mechanical and thermal properties of $Yb_2Si_2O_7$ [14], [61], [62].*

T (°C)	E (GPa)	ν	α (×10^{-6} K^{-1})	ρ (kg/m^3)	k (W/m·K)	C (J/g·K)	K_c (Mpa.m$^{1/2}$)	G_c (J/m^2)
25	90	0.27	4.1	5670	0.8646	0.33131	2.76	78.47
100	90	0.27	4.1	5670	0.8235	0.4106	2.76	78.47
200	90	0.27	4.1	5670	0.77638	0.46592	2.76	78.47
300	90	0.27	4.1	5670	0.74114	0.49719	2.76	78.47
400	90	0.27	4.1	5670	0.70406	0.51758	2.76	78.47

500	90	0.27	4.1	5670	0.68188	0.53233	2.76	78.47
600	90	0.27	4.1	5670	0.67816	0.54387	2.76	78.47
700	90	0.27	4.1	5670	0.69951	0.55344	2.76	78.47
800	90	0.27	4.1	5670	0.75459	0.56175	2.76	78.47
900	90	0.27	4.1	5670	0.84526	0.5692	2.76	78.47
1000	90	0.27	4.1	5670	0.97298	0.57606	2.76	78.47
1100	90	0.27	4.1	5670	1.14562	0.58249	2.76	78.47
1200	90	0.27	4.1	5670	1.36782	0.5886	2.76	78.47

Table 4: *Mechanical and thermal properties of Yb_2SiO_5 [61], [63], [64].*

T (^oC)	**E (GPa)**	**ν**	**α ($x10^{-6}$ K^{-1})**	**ρ (kg/m^3)**	**k (W/m·K)**	**C (J/g·K)**	**K_c ($Mpa.m^{1/2}$)**	**G_c (J/m^2)**
25	63	0.25	7.5	7070	0.67901	0.29435	1.97	41.84
100	63	0.25	7.5	7070	0.68767	0.35339	1.97	41.84
200	63	0.25	7.5	7070	0.68057	0.3958	1.97	41.84
300	63	0.25	7.5	7070	0.66716	0.42091	1.97	41.84
400	63	0.25	7.5	7070	0.66661	0.43817	1.97	41.84
500	63	0.25	7.5	7070	0.68348	0.45136	1.97	41.84
600	63	0.25	7.5	7070	0.70652	0.46225	1.97	41.84
700	63	0.25	7.5	7070	0.73434	0.47172	1.97	41.84
800	63	0.25	7.5	7070	0.76126	0.48028	1.97	41.84
900	63	0.25	7.5	7070	0.79459	0.48823	1.97	41.84
1000	63	0.25	7.5	7070	0.8454	0.49574	1.97	41.84

1100	63	0.25	7.5	7070	0.93955	0.50295	1.97	41.84
1200	63	0.25	7.5	7070	1.12579	0.50993	1.97	41.84

Table 5: *Mechanical and thermal properties of other EBC materials [62], [63], [65], [66].*

Material	**E (GPa)**	**ν**	**α ($\times 10^{-6}$ K^{-1})**	**ρ (kg/m^3)**	**k (W/m·K)**	**C (J/g·K)**	**K_c (Mpa. $m^{1/2}$)**	**G_c (J/m^2)**
α -cristobalite	65	-0.164	30	2000	2.69	0.741	0.77	8.87
β-cristobalite	70	-0.042	3.1	2000	2.69	0.741	0.77	8.87
Si	82	0.223	4.1	2329	124	0.794	1.58	28.93
SiC	430	0.14	4.67	3210	120	0.674	3.1	

4.3. Model Description

The study presents a comprehensive 2D time-dependent finite element model designed to simulate the behavior of a multi-layered EBC system subjected to thermal cycling. The geometry consists of five domains, each representing different materials and layers of the EBC system, as illustrated in Figure 13. These layers include a 250 µm thick $Yb_2Si_2O_7$ $Yb_2Si_2O_7$ topcoat, a 125 µm thick Si bond coat, and a 32 mm thick silicon carbide SiC substrate. While the actual topcoat/bond coat interface exhibits irregular and non-uniform roughness, and this is modelled as using a simplified sinusoidal function with an amplitude of 10 µm to capture undulation effects. The interfaces between the coating layers were modeled as perfect, assuming ideal bonding with full continuity of stresses and displacements. No interfacial slip, separation, or damage was considered during loading.

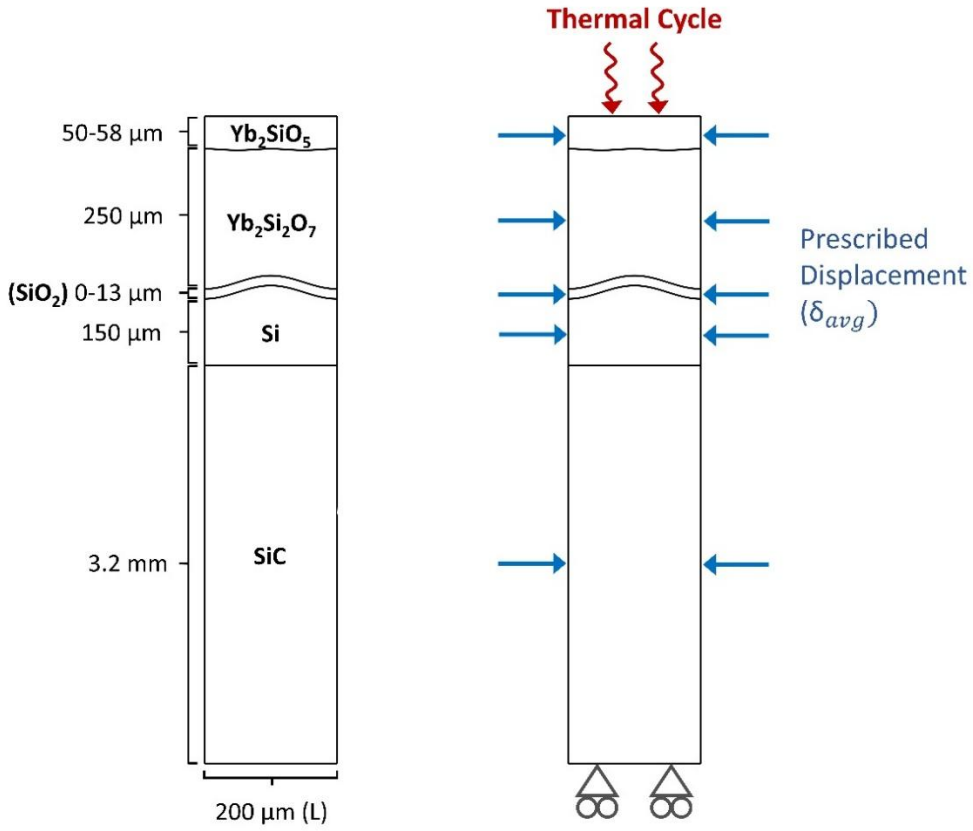

Figure 13: *Schematic illustration of $Yb_2Si_2O_7$/ Si EBC FEM geometry with boundary conditions.*

The boundary conditions applied to the system are critical to modelling the behavior under realistic operating conditions. The lateral boundaries of the model, shown in Figure 13, were constrained using a prescribed displacement (Eq. 15) based on the weighted average of thermal strains from all layers. This boundary condition approximates the net thermal expansion of the multilayer system, preventing artificial edge effects and accurately representing the in-plane constraints during thermal cycling. The lateral boundaries are also subjected to periodic boundary conditions, representing an infinitely long system, which reduces the need to model the entire geometry.

$$\delta_{avg} = \frac{\sum \alpha_i t_i}{\sum t_i} \cdot \frac{L}{2} . \Delta T \tag{15}$$

Where, δ_{avg} is the average thermal displacement, α_i and t_i are the CTE and thickness of layer i, *L* is the total in-plane width of the system, and ΔT is the temperature change with respect to the reference temperature (1316°C).

The top boundary is subjected to a thermal cycle, as shown in Figure 14, which ranges from 110°C to 1316°C with a dwell time of 1 hour at 1316 °C. This thermal cycling simulates the experimental conditions [14], [21], [34], [63] that the material is exposed to high temperatures during use. A reference temperature of 1316 °C is used for thermal expansion analysis, corresponding to the typical stabilization annealing temperature of the EBC system [14]. The system is assumed to be initially stress-free at this reference temperature, and the thermal stresses develop as the system cools to lower temperatures during thermal cycling. Additionally, the study assumes isotropic elasticity of materials subjected to generalized plane strain conditions, which simplifies the problem by assuming negligible deformation in the direction perpendicular to the 2D plane, making the simulation computationally efficient while still capturing critical physical phenomena.

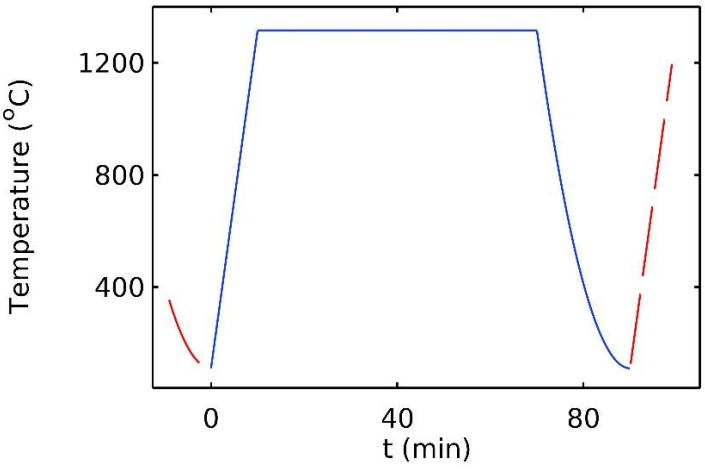

Figure 14: *A thermal cycle between 110°C and 1316°C.*

Figure 15 shows the unstructured mesh with second-order quadrilateral (quad) elements used in the model. The initial mesh includes 51,294 domain elements. Automatic Remeshing is

implemented in COMSOL to accommodate the evolving geometry due to the simulated growth of the TGO and Yb_2SiO_5 layers. Remeshing is triggered when the mesh quality drops below a threshold value of 0.2 to preserve numerical accuracy as the geometry evolves over time.

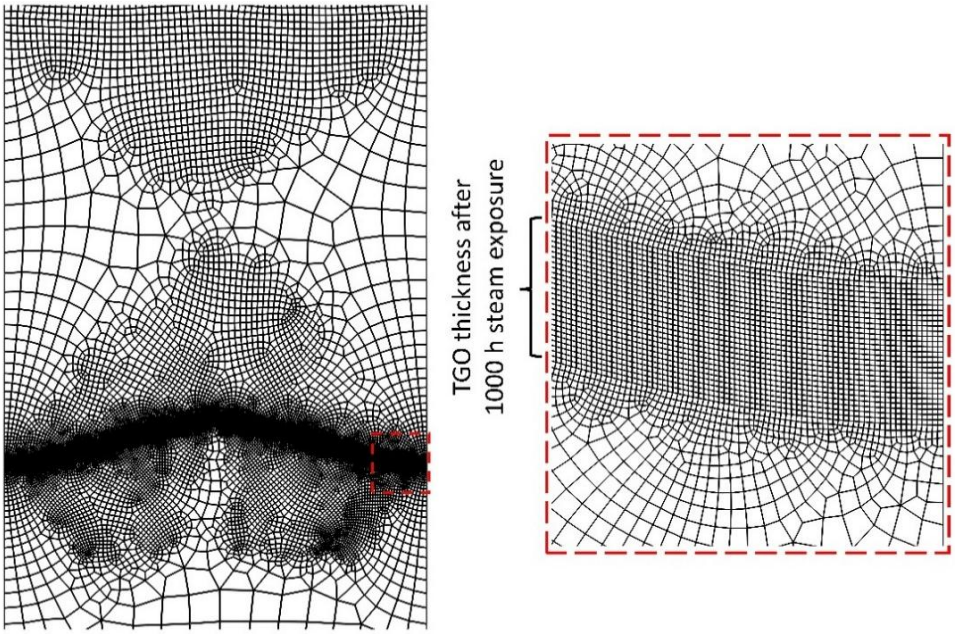

Figure 15: *FE mesh used for stress model showing high mesh density at the TGO domain.*

4.4. Phase Field Damage Model

To date, a number of numerical models and methods have been developed to study the material's failure behavior [39], such as the Virtual Crack Closure Technique (VCCT), the Cohesive Zone Model (CZM), and the eXtended Finite Element Method (XFEM). In these methods, the VCCT and CZM normally apply to the predefined cracks. Therefore, they are widely applied to interfacial delamination problems. The XFEM method predicts cracks independently of the mesh setup, allowing it to simulate the undefined crack problem within a solid.

In this study, the phase-field damage model is applied, which defines a sharp crack as a diffusive crack controlled by the phase field variable, ranging from 0 to 1. When the phase-field variable equals 1, the material is fully damaged; when it equals 0, it is intact. At the crack topology, the

variable equals 1 at the center of the crack surface and gradually moves to 0 at the width of the diffusive length scale [67]. In the present study, the characteristic length is set to $l = 0.2$ and a mesh size of 0.05 μm is maintained within the TGO. Miehe et al. [68], [69] introduced the phase field diffusive crack propagation method of finite element analysis without modelling discontinuities in the displacement field. This built-in feature in the COMSOL 6.3 Multiphysics simulation package includes the Structural Mechanics Module, Nonlinear Structural Materials Module, and Heat Transfer Module. These modules were implemented in conjunction with the TGO growth kinetics and creep models of each layer to study the EBC stress distribution and evolution, as well as crack nucleation and propagation.

Only the tensile part of the strain energy density drives crack evolution, preventing damage growth under compression. Furthermore, COMSOL enforces irreversibility of fracture. During unloading, the phase-field variable remains constant and cannot decrease, ensuring that damage does not heal and that the crack state evolves in a physically consistent manner.

5. Results and Discussion

5.1. Stress Distribution

The stress distribution within EBCs is crucial for understanding the mechanical response of the coating under high-temperature cycling and oxidation conditions, as well as for identifying potential failure mechanisms. This section presents key insights into how stresses develop and accumulate in the EBC, which are governed by numerous factors, including thermal expansion mismatch, thermal gradient, oxidation, creep, phase transformations, and the geometry of the coating interfaces. These findings are discussed in light of existing experimental studies to provide a deeper understanding of the mechanisms that drive stress accumulation and failure in EBCs. Figure 16 illustrates the distribution of plane stresses in the $Yb_2Si_2O_7$/Si EBC. Figure 17 presents

the variation of in-plane stresses through the coating thickness along the centerline of the EBC. The results correspond to the cooling stage at 110 °C after 10 cycles (1000 hours of steam exposure), at which point the TGO has reached a thickness of 13.42 µm**.**

In the multilayer $Yb_2Si_2O_7$/Si EBC system, stress distribution varies significantly across different layers, primarily due to mismatches in their CTE. Notably, the $Yb_2Si_2O_7$ topcoat, Si bond coat, and SiC substrate exhibit compressive stresses during cooling, owing to their relatively lower CTE values compared to the TGO and Yb_2SiO_5 layers, which experience tensile stresses. These contrasting stress states coexist in mechanical equilibrium, maintained in the simulation by a prescribed lateral boundary condition. This boundary condition, based on the weighted average of thermal strains from all layers, ensures the zero net force across the multilayer system during thermal cycling.

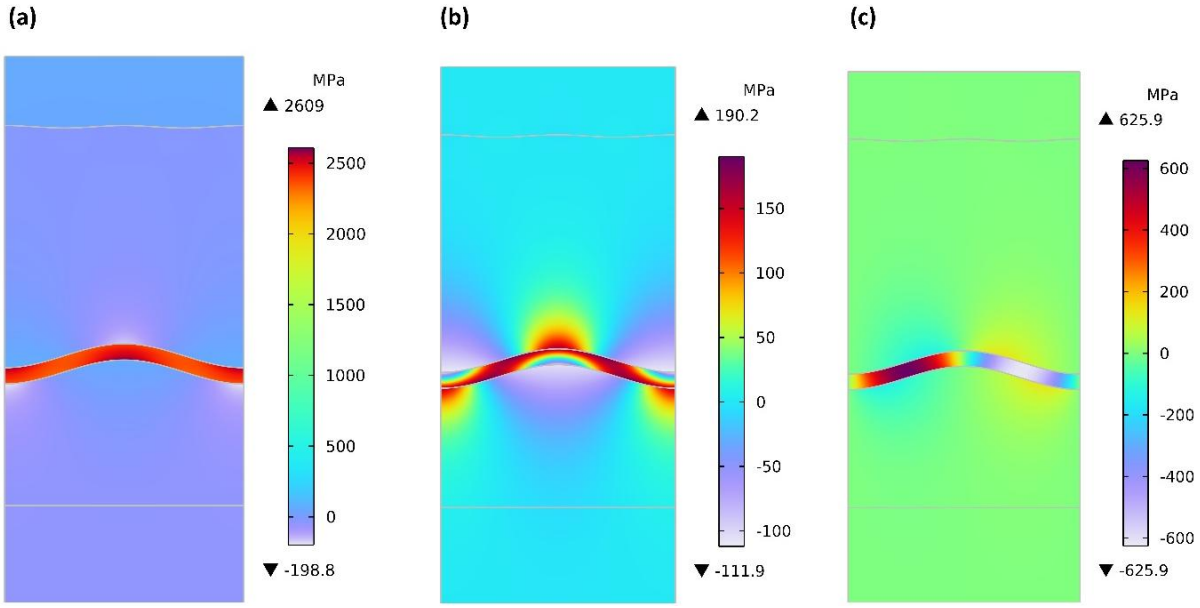

Figure 16: *In-plane stress distribution within $Yb_2Si_2O_7$/Si EBC at 110 °C after 1000 hours of steam exposure (a) σ_{11}, (b) σ_{22}, and (c) σ_{12} shear component.*

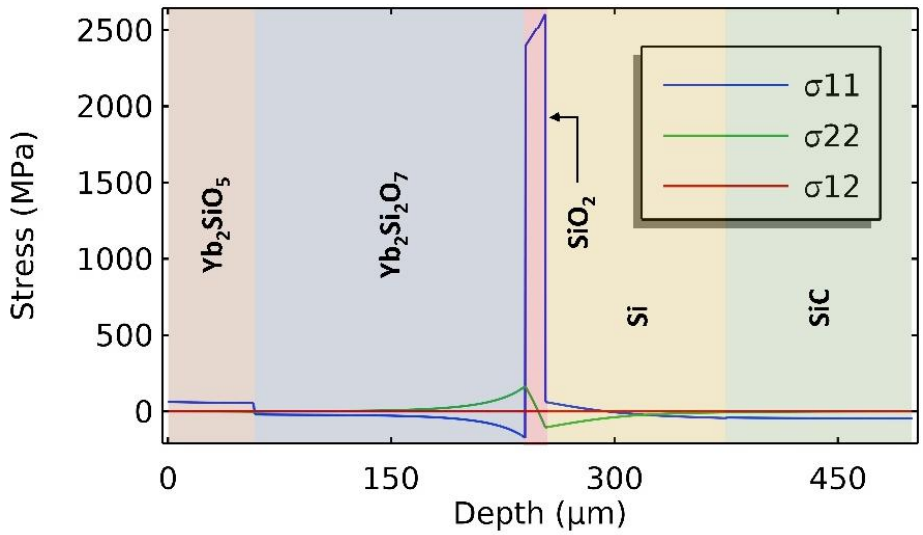

Figure 17: *In-plane stresses represented through the thickness of the EBC system at 110 °C after 1000 hours of steam exposure.*

The TGO is the region of primary interest in this study, as it exhibits the highest in-plane stress concentrations, which make it a likely site for crack initiation and delamination. The stress evolution within the TGO layer is governed by a complex interplay of oxidation growth, creep deformation, thermal mismatch and phase transformation. During high-temperature oxidation, the formation of SiO_2 results in a volumetric expansion of approximately 2.2 times [14], generating substantial growth-induced compressive stress. However, at elevated temperatures, the TGO undergoes significant time-dependent creep deformation, which facilitates stress relaxation. In the current simulations, the equivalent creep strain within the TGO reaches approximately 55%, indicating that a large fraction of the oxidation-induced compressive stress is relaxed during the isothermal hold.

Upon cooling, the TGO begins to accumulate tensile stress due to the combined effects of thermal mismatch and phase transformation. Specifically, the cristobalite in the TGO transforms from the β-phase to the α-phase, accompanied by a substantial increase in the CTE from ~$0.5 \times 10^{-6}\ K^{-1}$ to

~$30 \times 10^{-6}\,K^{-1}$. This causes TGO to contract significantly more than the surrounding layers but being constrained by them generates large internal tensile stresses during cooling. Moreover, this transformation also involves a ~5% volumetric shrinkage, which further contributes to the tensile stress buildup. As a result, the maximum in-plane tensile stress (σ_{11}) reaches ~2.6 GPa in the TGO at 110 °C, as shown in Figures 17-19. The variation of TGO stress (σ_{11}) with temperature during the cooling phase of the first thermal cycle at the TGO thickness of 4.24 μm is presented in Figure 18. Above the phase transformation temperature (~270ºC), the TGO stress is compressive due to the presence of the β -phase of the cristobalite [45]. The stress shifts from compression to tension at the transition temperature as the β-cristobalite converts to the α-phase during cooling. With continued cycling, σ_{11} gradually increases from ~2545 MPa after the first cycle (100 h) to ~2608 MPa after ten cycles (1000 h). The progressive increase in tensile stress with TGO growth is primarily due to the combined effects of volumetric shrinkage resulting from the β→α transformation of cristobalite and the constraint imposed by surrounding layers. As the TGO thickens during oxidation, a larger volume of material undergoes the phase transformation, generating additional shrinkage strain. Because this strain is constrained by the adjacent $Yb_2Si_2O_7$ and Si layers, the resulting in-plane stresses accumulate, leading to higher tensile stress (σ_{11}).

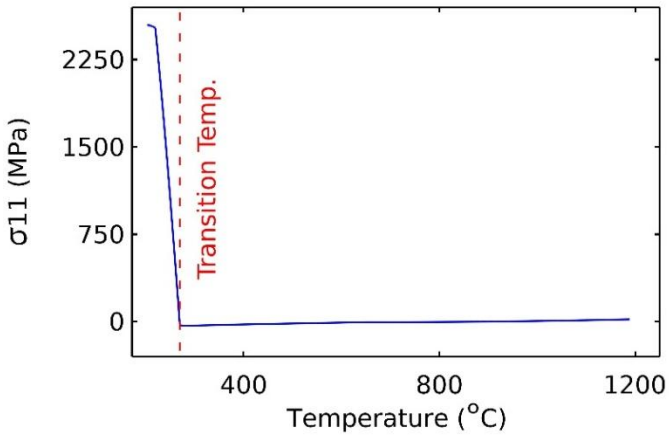

Figure 18: *Change in TGO stress (σ11) with temperature.*

The undulated interface geometry causes non-uniform stress distributions within the TGO layer. Localized stress concentrations predominantly develop at the peaks of the TGO/bond coat interface and the valleys of the topcoat/TGO interface, as the geometric curvature amplifies the lateral tensile stress (σ_{11})**.** In-plane shear (σ_{12}) and through-thickness normal (σ_{22}) stresses in the TGO are also highly sensitive to interface undulation. For a flat interface, these stress components remain negligible due to the uniform lateral deformation enforced by the prescribed displacement boundary condition. Without geometric misalignment, there is no mechanism to generate shear or through-thickness stresses. However, when interface undulation is introduced, the undulated geometry causes the dominant in-plane tensile stress (σ_{11}) to resolve into local tangential and normal components, resulting in the development of shear (σ_{12}) and through-thickness stresses (σ_{22}). As a result, maximum shear and through-thickness stresses occur in the off-peak regions (between peaks and valleys) of the TGO, where the undulation slope is the highest and the in-plane stress (σ_{11}) is more effectively resolved into normal and tangential components. As shown in Figure 19, for a 10 μm undulation amplitude, σ_{12} and σ_{22} reach approximately 625 MPa and 190 MPa, respectively. Importantly, to satisfy force balance within the TGO layer, σ_{12} and σ_{22} stress components occur in pairs of almost equal magnitude but opposite sign, tension and compression, ensuring a net-zero force.

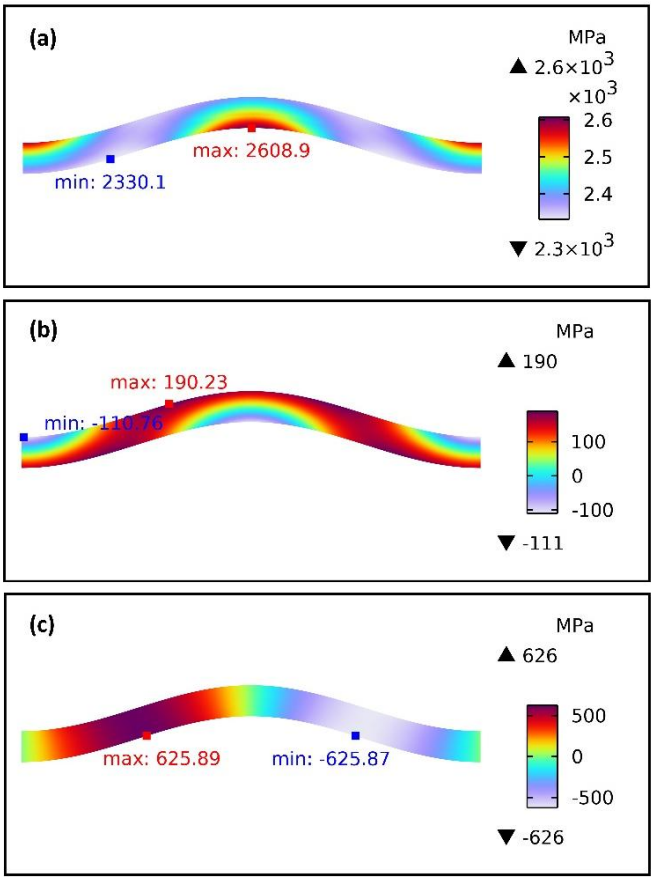

Figure 19: *In-plane stress distribution within the TGO at 110 °C after 1000 hours of steam exposure: (a) σ_{11}, (b) σ_{22}, and (c) σ_{12} shear components.*

The variation in stress distribution within the EBC highlights the complexity of the stress field across the multilayered system. In addition to the influence of interface undulations, the non-uniformity in stresses is also affected by the thermal gradient established across the coating thickness. Based on the thermal conductivity of the layers, the temperature decreases from the surface to the substrate as illustrated in Figure 20. This reduction in temperature lowers the corresponding thermal strain, which in turn contributes to variations in stress levels across the coating layers. Temperature gradients were incorporated in the present analysis through heat transfer boundary conditions. However, unlike in thermal TBCs, where steep temperature drops of several hundred degrees are sustained across the coating thickness, the thermal gradient in EBCs

is comparatively modest. Therefore, the independent effect of thermal gradient on stress distribution was not investigated in isolation in the present study.

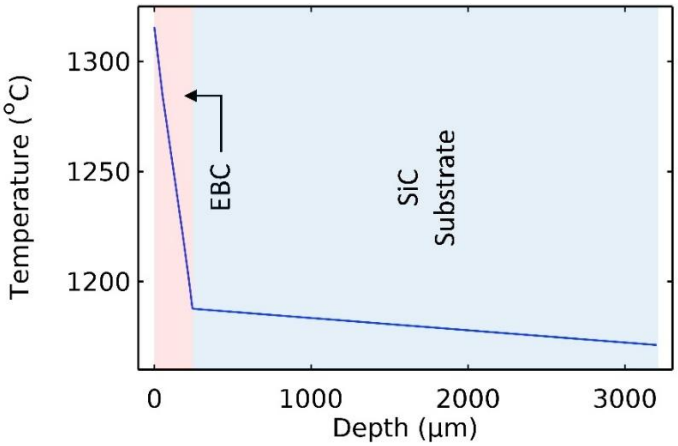

Figure 20: *Temperature gradient across multi-layered EBC and substrate.*

Overall, the stress distribution predicted for the $Yb_2Si_2O_7$/Si EBC in the present study is in alignment with the findings of Richards et al. [14], where the modelling in this work and the referenced study consider the same EBC system, similar stabilization temperatures and thermal cycling conditions. In both cases, the TGO experiences the highest tensile stresses, while the $Yb_2Si_2O_7$ topcoat, Si bond coat, and SiC substrate remain predominantly under compressive stress.

5.2. Elastic Energy Density and Evaluation of Energy Release Rate

The elastic strain energy density W was evaluated to quantify the stored mechanical energy available for fracture per unit volume in the EBC system. The spatial distribution of W within the TGO is illustrated in Figure 21. For the 10 μm interface undulation amplitude and a TGO thickness of 13.42 μm after 1000 hours of steam exposure, the maximum W values of approximately 116 MJ/m^3 were observed near the interface peaks and valleys, with noticeable gradients through the TGO thickness. These localized maxima in W correlate directly with stress concentration regions. W was negligible in the other EBC layers, and its magnitude remained nearly constant over each

thermal cycle. However, the total elastic strain energy stored in the TGO increases over time due to thickness growth, which increases the available volume for energy accumulation.

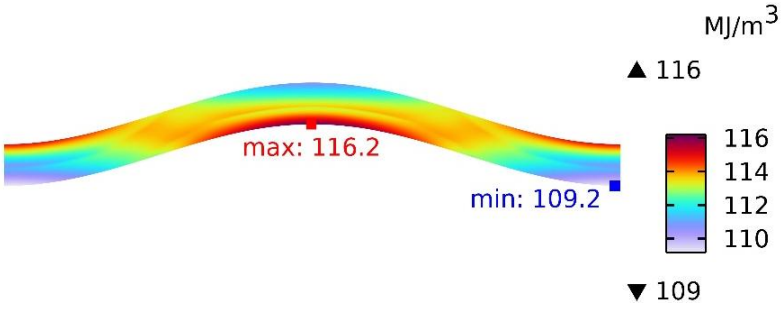

Figure 21: *Elastic strain energy density (W) distribution in the TGO after at 110°C after 1000 hours of steam exposure for a 10 µm interface undulation amplitude.*

According to Griffith's fracture criterion, crack propagation occurs when the locally stored elastic strain energy exceeds the critical energy required to create new fracture surfaces. In ceramic layers, tensile stresses are the primary driver for crack growth, promoting the opening of cracks perpendicular to the direction of the applied stress. The dominant lateral tensile stress (σ_{11}) therefore favours crack propagation normal to the interface, corresponding to Mode I fracture.

Figure 22 presents the Energy Release Rate (G) for cracks propagating normal to the interface, evaluated at peak and off-peak TGO locations using J-integral and Virtual Crack Extension (VCE) method in COMSOL. G value using VCE is determined from the change in the system's potential energy due to an infinitesimal crack extension, while for J-integral, G is based on the stress and strain fields near the crack tip, and it is a path-independent contour integral of the strain energy density. Pre-defined slit-type cracks, where the nodes on the two crack faces are geometrically coincident but not connected and are allowed to separate under loading, were inserted in the TGO. Finite element mesh were refined locally near the crack tips until the variation in G was less than 3%, and G was averaged over contours spanning 0.2–0.5 times the crack length. Maximum G

values of ~580 J/m² at peak locations and ~660 J/m² at off-peak locations were obtained at approximately 0.75% of the nominal crack length, after which *G* decreased as the crack approached the interface. Although *W* is concentrated at the peaks and valleys, the presence of gradients through the thickness at these locations reduces the effective energy available for crack growth. In contrast, off-peak regions exhibit a more uniform distribution of *W* through the thickness, resulting in a higher *G* and making crack growth more energetically favourable there.

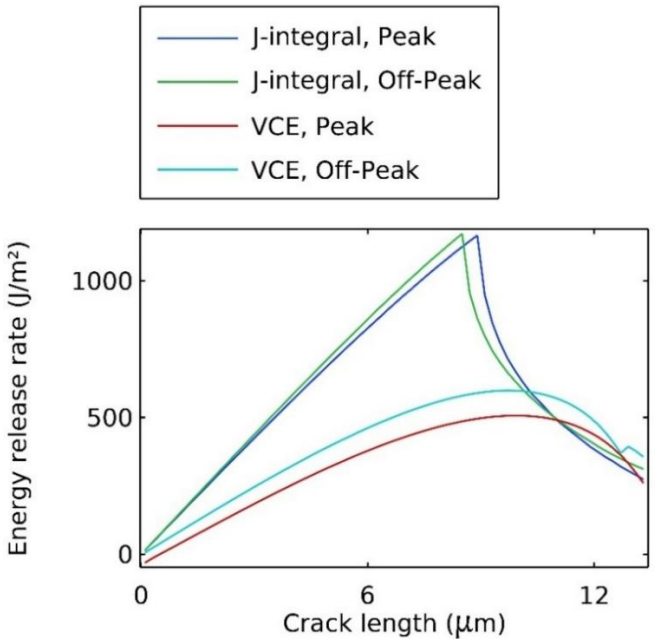

Figure 22: *Energy release rate (G) for cracks propagating normal to the interface at peak and off-peak TGO locations, calculated using J-integrals and Virtual Crack Extension (VCE) methods in COMSOL*

Figure 23 presents the Energy Release Rate (*G*) as a function of crack kink angle (θ) for two representative crack lengths within the TGO: a 5 μm crack with the crack tip well inside the TGO domain and a 10 μm crack with the crack tip near the TGO/$Yb_2Si_2O_7$ interface. For the shorter 5 μm crack, *G* attains its maximum at θ = 0°, indicating that vertical cracks at this stage preferentially propagate straight without deviation. In contrast, for the 10 μm crack located near the interface (~ 0.75% of the nominal crack length), *G*–θ curves exhibit two symmetric maxima at θ = ±35°, with

θ = 0° corresponding to a path normal to the interface. The reduction in G at θ = 0° for this case arises because the J-integral contour extends beyond the TGO into the $Yb_2Si_2O_7$, where compressive stresses suppress energy release. The presence of local maxima at ±35° suggests that cracks approaching the interface are energetically favoured to bifurcate toward these angles. A similar effect is expected near the TGO/Si interface, where compressive stresses in the Si bond coat likewise limit vertical crack penetration. Successive kinking events progressively align the crack path parallel to the interface, promoting a transition from vertical crack growth to delamination-dominated fracture in the later stages.

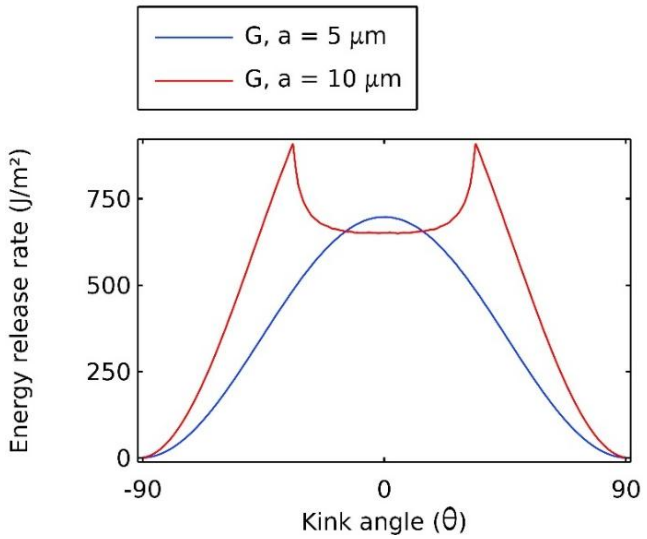

Figure 23: *Energy Release Rate (G) as a function of crack kink angle (θ) for 5 μm and 10 μm crack lengths.*

5.3. Crack Nucleation, Propagation and Failure Mechanism Using the Phase Field Damage Model

In this section, the fracture behavior of $Yb_2Si_2O_7$/Si EBCs was investigated using a phase-field formulation, in which cracks are represented as diffuse interfaces. The method minimizes a total energy functional that incorporates both the bulk elastic strain energy and the fracture surface energy, allowing for the simulation of crack nucleation and growth without the need for explicit crack tracking. To enhance numerical accuracy while maintaining computational efficiency, the

phase field was coupled with adaptive mesh refinement (AMR), providing high resolution near evolving crack fronts.

A parametric study was performed for varying TGO thicknesses, with no pre-inserted cracks, to evaluate spontaneous crack nucleation and growth mechanisms. In all simulations, no cracks were observed in the Yb_2SiO_5 layer under the current thermal cycling conditions, despite experimental reports of vertical cracks in this layer [14]. This discrepancy is likely due to the high porosity of Yb_2SiO_5 in service, where pores act as preferential crack initiation sites. This effect is not captured in the present simulation.

Figure 24 shows the phase field simulation results for TGO of varying thickness at the end of the cooling period of the thermal cycle. In the TGO layer, no cracking occurred for a 1 μm thickness, as shown in Figure 24 (a), consistent with experimental observations that crack nucleation is not energetically favourable below ~1.5 μm [14]. The strain energy is sufficient to initiate local damage ($d \approx 0.9$), but not sufficient to drive crack propagation due to limited TGO volume. Vertical cracks were first observed in a 2 μm-thick TGO sample, as shown in Figure 24(b). Since the length of the individual vertical cracks is short, multiple vertical cracks are formed simultaneously to relieve the stored elastic energy in the layer, resulting in a higher vertical crack density. In thicker TGO layers, vertical cracks are longer and relieve more stored energy as they propagate through the TGO thickness. As these longer cracks approach the interface, it becomes energetically favourable for cracks to bifurcate and propagate along the interface. This bifurcation behavior is consistent with our J-integral results, which showed that cracks approaching the interface experience the reduced G at $\theta = 0°$ but higher G at $\pm 35°$, favouring kinking and deflection.

Larger stored strain energy, resulting from increasing TGO thickness, promoted longer and more extensive delamination parallel to the interface, while the density of vertical cracks decreased.

Interestingly, the first cracks nucleated preferentially at off-peak locations of the TGO rather than at the geometric peaks/valleys. Subsequent cracking initiated in the vicinity of these off-peak cracks, and later appeared near peaks and valleys, Figure 24 (c) to (f). This behavior correlates with the calculated energy release rate (G) distribution, which was found to be higher at off-peak positions due to through-thickness gradients in stored strain energy. It is interesting to note that the calculated crack nucleation and propagation pattern shown in Figure 24 by the phase field damage variable is similar to those of the experimentally observed TGO crack behavior of Figures 13 and 16 via scanning electron microscope (SEM) in [34].

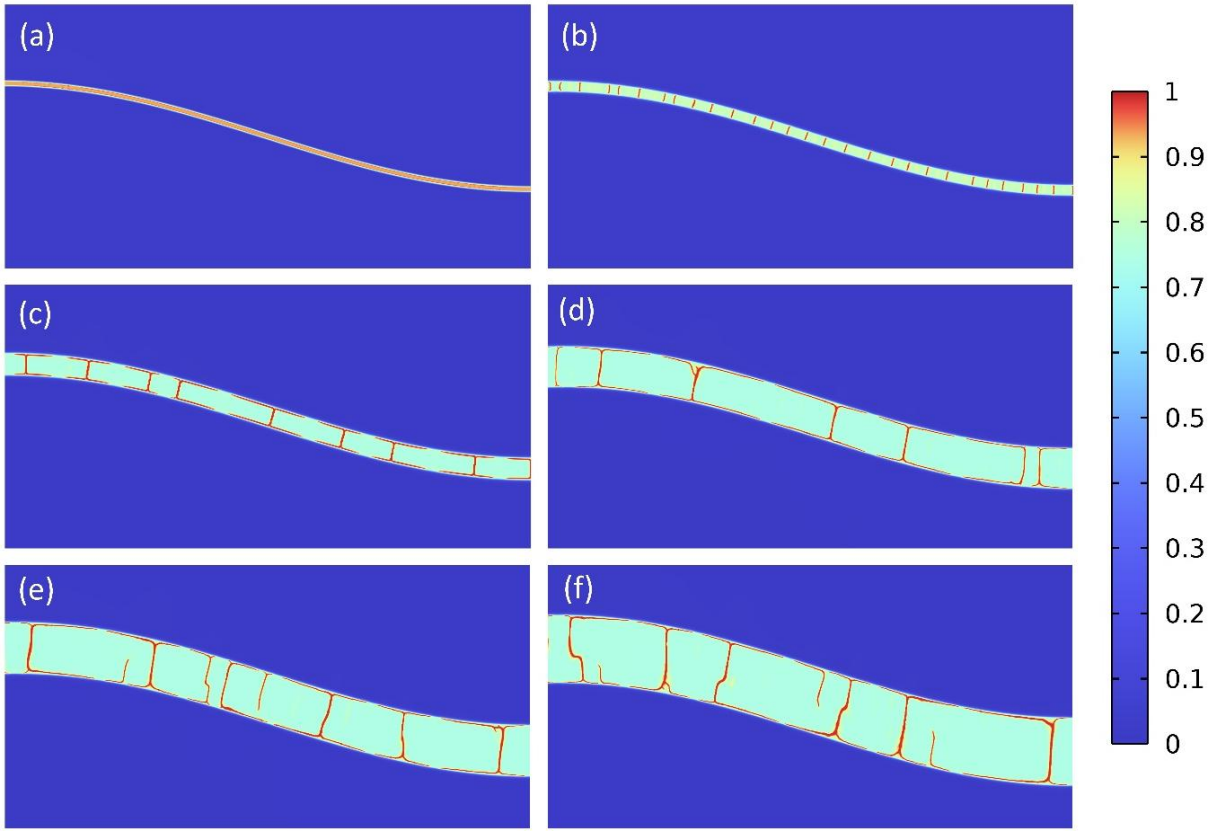

Figure 24: *Parametric phase field simulation of TGO layer with 10 μm undulation amplitude after cooling at the thickness of (a) 1 μm, (b) 2 μm, (c) 4 μm, (d) 8 μm, (e) 10 μm, and (f) 13 μm.*

Figure 25 shows the equivalent von Mises stress computed from the damaged stress tensor, $\sigma_d=(1-d)\ \sigma_{un}$, where *d* is the phase-field damage variable and σ_{un} is the undamaged (effective) stress. In this formulation, σ_d represents the actual stress the material can carry after local fracture. It decreases progressively in regions where cracks nucleate and propagate, and vanishes in fully fractured zones, thereby enforcing traction-free crack faces. At the end of the cooling cycle, the TGO without damage experiences a peak stress of ~2.6 GPa, whereas with the damage model, the peak von Mises stress is reduced to ~500 MPa and concentrated at the interfaces, reflecting stress relaxation due to fracture. Similar to Figure 24, the narrower white-coloured regions in Figure 25 show the crack paths after implementing the phase field damage model. They show a similar pattern to Figure 24, and also similar to that of the experimentally observed TGO crack pattern of Figures 23 and 26 in [13].

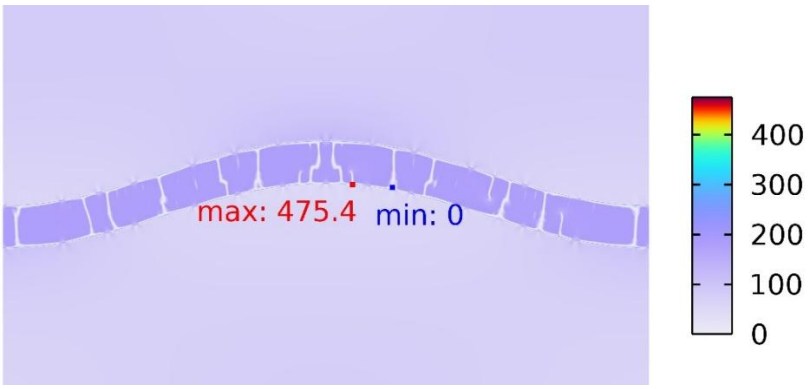

Figure 25: *Distribution of von Mises stress in the damaged TGO layer, showing stress relaxation due to fracture.*

Figure 26 illustrates the evolution of the maximum damaged von Mises (VM) stress for different TGO thicknesses during the cooling cycle, showing an initial increase due to thermal contraction and phase transformation, followed by a decrease as damage develops and the material loses stiffness. The stress evolution for von Mises in the TGO of 13.42 µm thickness with no fracture (damage deactivated) is also illustrated with a dashed line for reference. Confirming the phase

field results for 1 μm thickness, stress relaxes due to local softening, but a continuous crack path never develops. For cracks exceeding 2 μm thickness, a sharp peak of ~1500 MPa marks the onset of damage initiation, after which the stress rapidly drops to ~500 MPa due to unstable crack propagation. This is followed by a steady decline, indicating further fracture progresses in a more stable manner as cracks propagate and redistribute stresses.

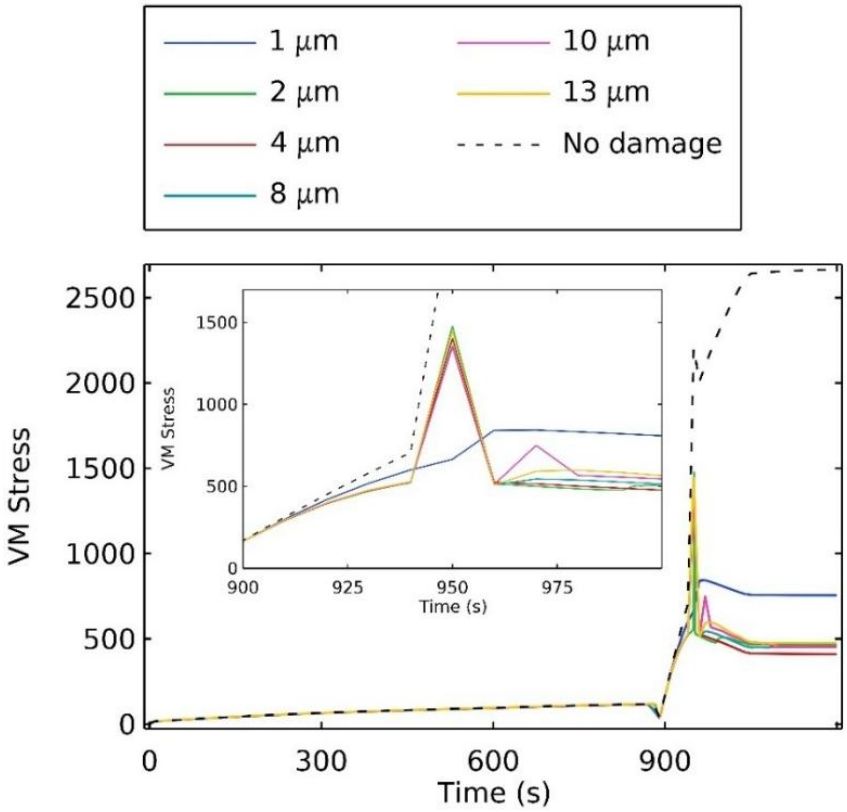

Figure 26: *Evolution of von Mises stress during the cooling period for varying TGO thicknesses. The region between 900 and 1000 s is enlarged in the figure to show detailed stress variations. Dashed line represent the VM stress without damage.*

In these phase-field simulations, the TGO growth kinetics were not modelled. Instead, TGO thickness was varied parametrically to examine its effect on fracture nucleation and propagation. The parametric results indicate that thicker TGO layers experience lower vertical crack density and more extensive delamination damage. However, the exact interaction between TGO growth

kinetics and the existing cracks depends on detailed stress redistribution and would require a fully coupled growth–fracture simulation to quantify accurately.

The aforementioned results indicate that EBC's failure is likely to initiate through the bifurcation of vertical channel cracks near the two interfaces, followed by the coalescence of closely spaced cracks and eventual coating spallation. However, the present phase-field approach primarily captures fracture within the TGO and does not explicitly model interfacial separation governed by adhesion properties. Incorporating a CZM would further enable explicit representation of the interface traction–separation behavior, allowing for more accurate simulation of interfacial delamination. Such a combined approach would provide a more complete understanding of the competition between TGO cracking and interfacial delamination, leading to improved predictive capability for exploring EBC failure mechanisms.

5.4. Effect of Interface Undulation on EBC Degradation

To further examine the influence of interface morphology on the degradation of EBC systems, a parametric study was conducted focusing on the TGO–bond coat and TGO–topcoat interfaces. The methodology follows the same approach established in the preceding sections. Four morphology configurations were considered, defined by an undulation ratio (amplitude-to-wavelength ratio): 0 (flat interface), 0.05 (10 μm amplitude, 200 μm wavelength), 0.10 (10 μm amplitude, 100 μm wavelength), and 0.15 (10 μm amplitude, 66.6 μm wavelength). The study evaluated and compared stress distributions, fracture-driving forces, and damage evolution for these interface geometries. All results are reported at the TGO thickness of 13.42 μm, corresponding to 1000 hours of steam cycling or 10 thermal cycles (accelerated).

Figure 27 presents the distribution of stress components σ_{11}, σ_{22}, and σ_{12} within the TGO layer after 10 thermal cycles for different interface undulation ratios (0, 0.05, 0.10, and 0.15). The in-plane stress σ_{11} rises from approximately 2.51 GPa (for a flat interface) to 2.94 GPa at an undulation ratio of 0.15, indicating increasing localization near the peaks and valleys created by sharper curvatures. The stress gradients through the TGO thickness at these localized regions also become significantly steeper with increasing undulation.

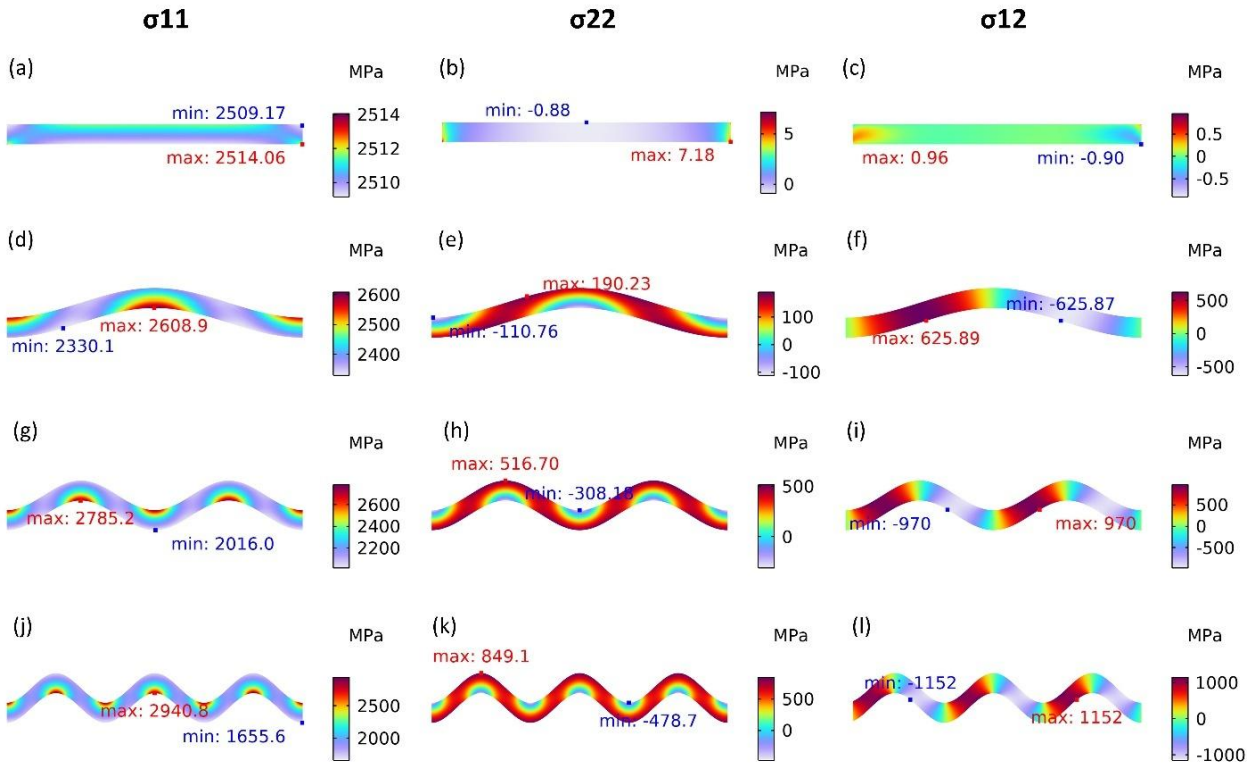

Figure 27: *Stress distributions within the TGO after 10 thermal cycles for four interface undulation ratios (0, 0.05, 0.10, 0.15). (a–d) in-plane normal stress σ_{11}, (e–h) through-thickness normal stress σ_{22}, and (i–l) in-plane shear stress σ_{12}.*

Notably, the through-thickness normal stress σ_{22} and the in-plane shear stress σ_{12} exhibit significant increases as the undulation ratio grows. The maximum tensile values of σ_{22} and σ_{12}

increase from negligible levels for a flat interface to approximately 849 MPa and 1150 MPa, respectively, at 0.15 undulation ratio, and are predominantly concentrated in off-peak regions of the TGO. This behavior is attributed to stress transformation arising from the local reorientation of stresses at steep interface slopes. These results confirm that higher undulation ratios amplify stress localization at the peaks and stress transformation at the slopes that promote stronger mixed-mode loading conditions.

As shown by the stress intensity factor analysis in Figure 28, evaluated at the TGO off-peak region over incremental crack lengths, fracture driving forces progressively shift in mode mixity with increasing undulation. The Mode I SIF (K_I) decreases from approximately 6.4 MPa·√m for a flat interface to about 5.2 MPa·√m at an undulation ratio of 0.15, while the Mode II component (K_{II}) rises from nearly zero (pure Mode I fracture) to approximately 1.4 MPa·√m. Although Mode I remains dominant, the relative increase in Mode II reflects stronger interfacial shear interactions at higher undulation ratios, producing a transition toward mixed-mode loading. This shift is directly linked to the concurrent rise in through-thickness normal (σ_{22}) and shear (σ_{12}) stress components induced by undulation. The amplified shear contribution thereby modifies fracture path selection by enhancing the mixed-mode fracture driving force and promoting interfacial (delamination) crack propagation within the TGO.

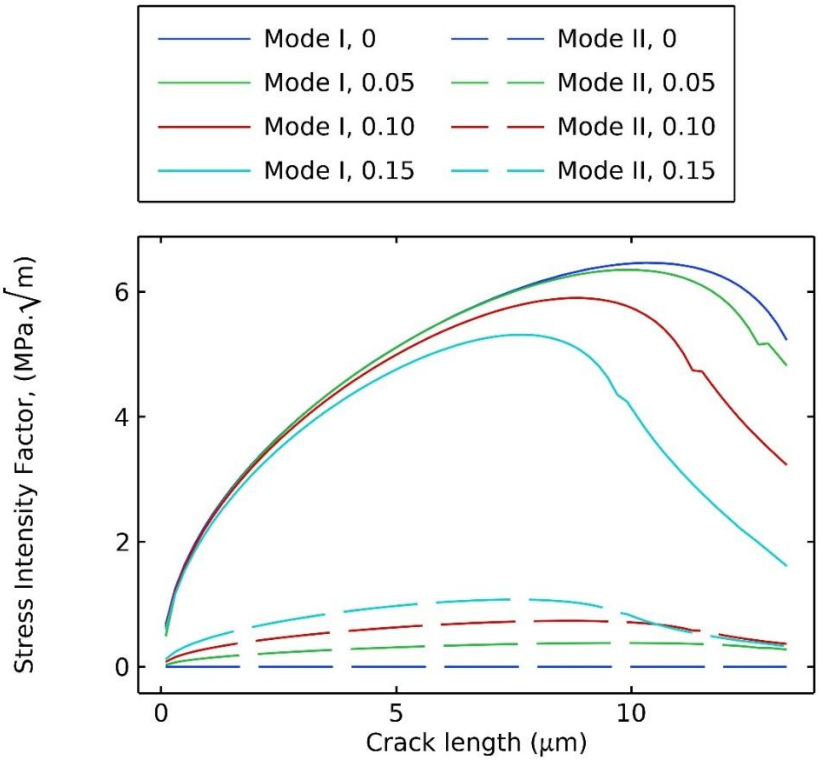

Figure 28: *Mode I (K_I) and Mode II (K_{II}) stress intensity factor evaluated at TGO off-peaks over incremental crack length for TGO thickness of 13.42 μm and undulation ratio = 0, 0.05, 0.10, and 0.15.*

Phase-field results shown in figure 29 corroborate these observations, reveling a clear dependence of crack initiation and propagation on interface morphology. For a flat interface, vertical cracks are distributed relatively uniformly across the TGO layer, whereas for undulated interfaces they predominantly localize in off-peak regions. Furthermore, the extent of interfacial delamination was markedly more severe as the undulation ratio increased. At higher undulation ratios (0.10 and 0.15), vertical cracking becomes more suppressed, with crack propagation dominated by pronounced interfacial delamination initiated through bifurcation of existing vertical cracks due to increased mixed mode loading conditions. This progressive damage eventually leads to near-complete coating spallation at 0.15 after 1000 hours of thermal cycling. The observed transition from predominantly vertical cracking to extensive interfacial delamination therefore reflects a

fundamental shift in the fracture driving mechanism, governed by changes in the stress distribution induced by interface undulation.

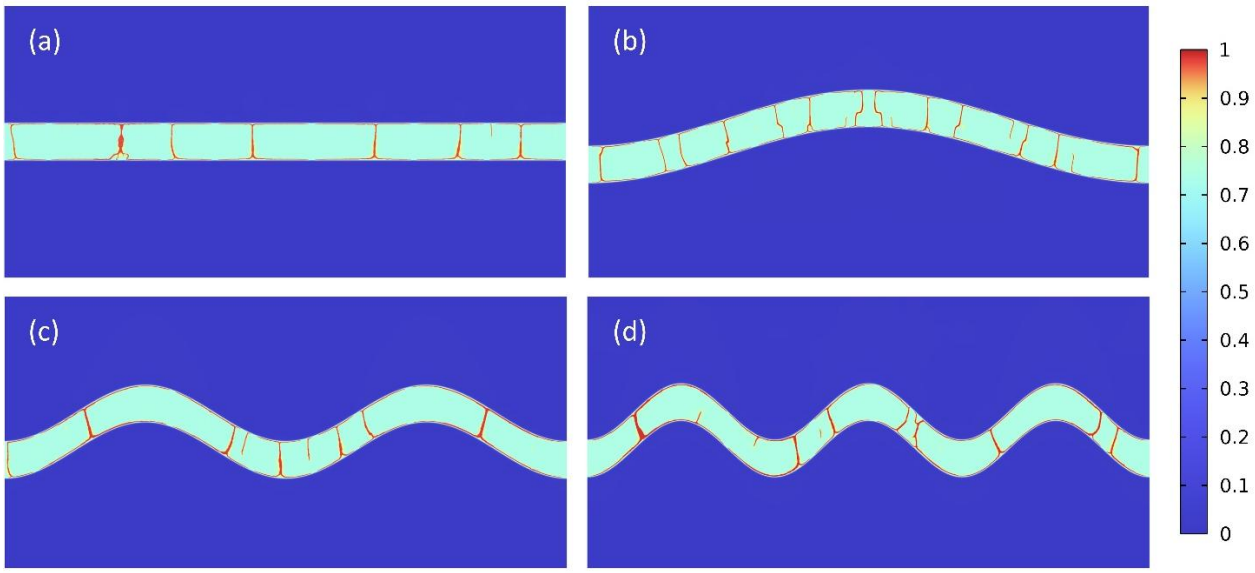

Figure 29: *Phase-field damage after 10 thermal cycles for: (a) undulation = 0; (b) undulation = 0.05; (c) undulation = 0.10; (d) undulation = 0.15.*

Overall, these findings highlight the critical role of interface morphology in governing damage evolution of TGO layers under cyclic thermal loading and in determining the service life of EBCs. Further research is needed to develop methods for producing smoother interfaces, which could include advanced polishing techniques, controlled deposition methods, and optimization of coating process parameters.

Methodological Note: Strain-based Initialization

Direct transfer of stress and displacements from the time-dependent stress analysis to a stationary model for energy release rate (G) and stress intensity factor (SIF) evaluations were not feasible. At the initial stage, the TGO thickness is negligible, preventing the introduction of a crack seed in the undeformed configuration. By the final time-step, the TGO growth produces large

deformations and geometry changes, and remeshing of the deformed geometry is required to introduce the crack seed. This remeshing alters the mesh topology, preventing one-to-one mapping of stresses and displacements from the original time-dependent solution. Attempts to interpolate stresses across meshes resulted in non-physical distributions and poor solver convergence. To overcome these limitations, the average strain in each domain at the selected time step was extracted from the time-dependent simulation and imposed as an initial strain in the stationary model. This approach preserves the overall stress state with high fidelity, resulting in only a 3.8% deviation from the transient solution, and provides a consistent basis for ERR/SIF calculations.

In addition, although the thermo-mechanical stress analysis in this study accounts for the time-dependent growth of the TGO, the phase-field fracture calculations are performed on fixed TGO thicknesses extracted at selected time steps (i.e., at the end of dwell periods in the thermal cycle). Damage is then evaluated during the subsequent cooling cycle, during which the TGO thickness is held constant. Integrating dynamic TGO growth with a phase-field fracture model would require simultaneously resolving moving interfaces/boundaries and crack evolution, resulting in a computationally demanding system. The remeshing required to accommodate continuous TGO growth also disrupts the continuity of displacement and phase-field variables, leading to numerical instability. By freezing the TGO geometry and applying the strain state obtained from the initial damage-free transient solution, the model captures the essential fracture-driving stresses while avoiding the complexity and instability associated with a fully coupled, dynamically evolving TGO–phase-field formulation.

6. Conclusion

This thesis systematically investigated the degradation and failure mechanisms of bi-layer $Yb_2Si_2O_7$/Si environmental barrier coatings (EBCs) applied on SiC substrate under realistic gas turbine operating conditions. A comprehensive multi-physics finite element framework was developed to simulate in-service behavior by integrating thermal cycling, high-temperature creep, oxide growth kinetics, phase transformations, and phase-field fracture modeling.

The finite element analyses showed excellent agreement with experimental observations and confirmed that tensile stresses within the TGO layer are the primary drivers of coating failure. Vertical cracks nucleate within the TGO and propagate through the oxide layer, where they bifurcate near the $Yb_2Si_2O_7$/TGO and Si/TGO interfaces and extend along these boundaries. Progressive crack coalescence promotes interfacial delamination and eventual coating spallation, consistent with experimental evidence. Parametric studies revealed that increasing TGO thickness leads to longer cracks with reduced crack density but more severe interfacial delamination. Furthermore, interface morphology was found to play a critical role in stress localization and fracture path selection. Increasing interface undulation amplifies the in-plane tensile stress (σ_{11}) at peaks and enhances the through-thickness (σ_{22}) and shear (σ_{12}) stresses at off-peak regions, thereby intensifying mixed-mode loading and accelerating delamination. Severe undulation conditions ultimately resulted in near-complete coating spallation after 1000 hours of thermal cycling.

Overall, this work establishes a robust analytical and predictive modeling framework capable of capturing the coupled thermo-mechanical, oxidation, and fracture processes governing EBC degradation. The results provide mechanistic insight into crack initiation, propagation, and spallation, and identify key controlling parameters—TGO thickness and interface morphology—

that dictate coating lifetime. Furthermore, this framework serves as a predictive tool to guide the design and optimization of next-generation EBC architectures and materials for improved durability in turbine environments.

7. Future Work

Building on the conclusions of this study, future work should aim to validate and extend the present findings through targeted experimental and modeling developments. Since the simulations revealed that oxide growth and interface undulation intensify stress localization and promote delamination, efforts should focus on reducing oxidation and refining deposition quality. Controlling oxide growth through optimized topcoat and bond-coat compositions, or by introducing oxidation-resistant intermediate layers, could limit oxide growth and reduce stress accumulation during thermal cycling. At the same time, improving APS deposition parameters such as torch power, particle velocity, and stand-off distance could yield denser coatings with reduced porosity, thereby minimizing oxygen ingress and subsequent TGO formation. Achieving smoother and more uniform interfaces through such refinements, or by exploring alternative deposition methods like PS-PVD or EB-PVD, would help suppress localized σ_{22} and σ_{12} stresses, ultimately enhancing coating durability and delaying damage initiation.

From a modeling standpoint, future studies should focus on coupling the phase-field method with CZM to more accurately capture interfacial delamination. Such integration would enable explicit representation of interfacial strength and traction–separation behavior, allowing more realistic simulation of crack bifurcation and sliding along the TGO interface. Additionally, incorporating oxygen diffusion into the model would provide a more complete description of oxidation-driven degradation under cyclic thermal conditions. Together, these advancements will enable a more

comprehensive understanding of failure mechanisms in EBC systems and support the development of coatings with improved durability and reliability.

8. References

[1] I. Spitsberg and J. Steibel, "Thermal and Environmental Barrier Coatings for SiC/SiC CMCs in Aircraft Engine Applications*," *Int. J. Appl. Ceram. Technol.*, vol. 1, no. 4, pp. 291–301, Oct. 2004, doi: 10.1111/j.1744-7402.2004.tb00181.x.

[2] N. P. Padture, "Advanced structural ceramics in aerospace propulsion," *Nat. Mater.*, vol. 15, no. 8, pp. 804–809, Aug. 2016, doi: 10.1038/nmat4687.

[3] A. G. Evans and D. B. Marshall, "Overview no. 85 The mechanical behavior of ceramic matrix composites," *Acta Metall.*, vol. 37, no. 10, pp. 2567–2583, Oct. 1989, doi: 10.1016/0001-6160(89)90291-5.

[4] J. A. Dever, M. V. Nathal, and J. A. DiCarlo, "Research on High-Temperature Aerospace Materials at NASA Glenn Research Center," *J. Aerosp. Eng.*, vol. 26, no. 2, pp. 500–514, Apr. 2013, doi: 10.1061/(ASCE)AS.1943-5525.0000321.

[5] J. Xu, V. K. Sarin, S. Dixit, and S. N. Basu, "Stability of interfaces in hybrid EBC/TBC coatings for Si-based ceramics in corrosive environments," *Int. J. Refract. Met. Hard Mater.*, vol. 49, pp. 339–349, Mar. 2015, doi: 10.1016/j.ijrmhm.2014.08.013.

[6] K. N. Lee *et al.*, "Upper Temperature Limit of Environmental Barrier Coatings Based on Mullite and BSAS," *J. Am. Ceram. Soc.*, vol. 86, no. 8, pp. 1299–1306, Aug. 2003, doi: 10.1111/j.1151-2916.2003.tb03466.x.

[7] M. Białas, "Finite element analysis of stress distribution in thermal barrier coatings," *Surf. Coat. Technol.*, vol. 202, no. 24, pp. 6002–6010, Aug. 2008, doi: 10.1016/j.surfcoat.2008.06.178.

[8] L. Wang, Y. Wang, X. G. Sun, J. Q. He, Z. Y. Pan, and C. H. Wang, "Finite element simulation of residual stress of double-ceramic-layer La2Zr2O7/8YSZ thermal barrier coatings using birth and death element technique," *Comput. Mater. Sci.*, vol. 53, no. 1, pp. 117–127, Feb. 2012, doi: 10.1016/j.commatsci.2011.09.028.

[9] Q. M. Yu, L. Cen, and Y. Wang, "Numerical study of residual stress and crack nucleation in thermal barrier coating system with plane model," *Ceram. Int.*, vol. 44, no. 5, pp. 5116–5123, Apr. 2018, doi: 10.1016/j.ceramint.2017.12.112.

[10] N. Nayebpashaee, S. H. Seyedein, M. R. Aboutalebi, H. Sarpoolaky, and S. M. M. Hadavi, "Finite element simulation of residual stress and failure mechanism in plasma sprayed thermal barrier coatings using actual microstructure as the representative volume," *Surf. Coat. Technol.*, vol. 291, pp. 103–114, Apr. 2016, doi: 10.1016/j.surfcoat.2016.02.028.

[11] A. Moridi, M. Azadi, and G. H. Farrahi, "Thermo-mechanical stress analysis of thermal barrier coating system considering thickness and roughness effects," *Surf. Coat. Technol.*, vol. 243, pp. 91–99, Mar. 2014, doi: 10.1016/j.surfcoat.2012.02.019.

[12] M. Rezvani Rad, G. H. Farrahi, M. Azadi, and M. Ghodrati, “Stress analysis of thermal barrier coating system subjected to out-of-phase thermo-mechanical loadings considering roughness and porosity effect,” *Surf. Coat. Technol.*, vol. 262, pp. 77–86, Jan. 2015, doi: 10.1016/j.surfcoat.2014.12.016.

[13] K. N. Lee, J. I. Eldridge, and R. C. Robinson, “Residual Stresses and Their Effects on the Durability of Environmental Barrier Coatings for SiC Ceramics,” *J. Am. Ceram. Soc.*, vol. 88, no. 12, pp. 3483–3488, Dec. 2005, doi: 10.1111/j.1551-2916.2005.00640.x.

[14] B. T. Richards, K. A. Young, F. De Francqueville, S. Sehr, M. R. Begley, and H. N. G. Wadley, “Response of ytterbium disilicate–silicon environmental barrier coatings to thermal cycling in water vapor,” *Acta Mater.*, vol. 106, pp. 1–14, Mar. 2016, doi: 10.1016/j.actamat.2015.12.053.

[15] B. T. Richards, S. Sehr, F. De Franqueville, M. R. Begley, and H. N. G. Wadley, “Fracture mechanisms of ytterbium monosilicate environmental barrier coatings during cyclic thermal exposure,” *Acta Mater.*, vol. 103, pp. 448–460, Jan. 2016, doi: 10.1016/j.actamat.2015.10.019.

[16] B. T. Richards, D. Zhu, L. J. Ghosn, and H. N. G. Wadley, “Mechanical Properties of Air Plasma Sprayed Environmental Barrier Coating (EBC) Systems: Preliminary Assessments,” in *Ceramic Engineering and Science Proceedings*, 1st ed., W. M. Kriven, J. Wang, D. Zhu, and T. Fischer, Eds., Wiley, 2015, pp. 219–237. doi: 10.1002/9781119211747.ch18.

[17] C. M. Heveran, J. Xu, V. K. Sarin, and S. N. Basu, “Simulation of stresses in TBC–EBC coating systems for ceramic components in gas turbines,” *Surf. Coat. Technol.*, vol. 235, pp. 354–360, Nov. 2013, doi: 10.1016/j.surfcoat.2013.07.066.

[18] A. Abdul-Aziz and R. T. Bhatt, “Modeling of thermal residual stress in environmental barrier coated fiber reinforced ceramic matrix composites,” *J. Compos. Mater.*, vol. 46, no. 10, pp. 1211–1218, May 2012, doi: 10.1177/0021998311414950.

[19] G. Fang, J. Ren, J. Shi, X. Gao, and Y. Song, “Thermal Stress Analysis of Environmental Barrier Coatings Considering Interfacial Roughness,” *Coatings*, vol. 10, no. 10, p. 947, Sept. 2020, doi: 10.3390/coatings10100947.

[20] Kawai *et al.*, “Crack Initiation Criteria in EBC under Thermal Stress,” *Coatings*, vol. 9, no. 11, p. 697, Oct. 2019, doi: 10.3390/coatings9110697.

[21] Y. Huang, Z. Wei, Q. Zhang, H. Cai, X. Han, and X. Dong, “Comprehensive understanding of coupled stress characteristics in ytterbium disilicate environmental barrier coatings undergoing corrosion transformation and thermal cycling,” *Ceram. Int.*, vol. 48, no. 17, pp. 25528–25537, Sept. 2022, doi: 10.1016/j.ceramint.2022.05.232.

[22] T.-L. Cheng, F. Xue, Y. Lei, R. P. Oleksak, Ö. N. Doğan, and Y.-H. Wen, “Phase-field modeling of thermally-grown oxide and damage evolution in environmental barrier coatings,” *Acta Mater.*, vol. 284, p. 120571, Jan. 2025, doi: 10.1016/j.actamat.2024.120571.

[23] K. N. Lee, D. Zhu, and R. S. Lima, “Perspectives on Environmental Barrier Coatings (EBCs) Manufactured via Air Plasma Spray (APS) on Ceramic Matrix Composites (CMCs): A Tutorial Paper,” *J. Therm. Spray Technol.*, vol. 30, no. 1–2, pp. 40–58, Jan. 2021, doi: 10.1007/s11666-021-01168-0.

[24] K. N. Lee, D. Zhu, and R. S. Lima, “Perspectives on Environmental Barrier Coatings (EBCs) Manufactured via Air Plasma Spray (APS) on Ceramic Matrix Composites (CMCs): A Tutorial Paper,” *J. Therm. Spray Technol.*, vol. 30, no. 1–2, pp. 40–58, Jan. 2021, doi: 10.1007/s11666-021-01168-0.

[25] J. H. Perepezko, “The Hotter the Engine, the Better,” *Science*, vol. 326, no. 5956, pp. 1068–1069, Nov. 2009, doi: 10.1126/science.1179327.

[26] A. H. Lefebvre and D. R. Ballal, *Gas Turbine Combustion*, 0 ed. CRC Press, 2010. doi: 10.1201/9781420086058.

[27] Rolls-Royce Limited and Rolls-Royce Plc, Eds., *The jet engine*, 6. ed. London: Rolls-Royce plc, 2005.

[28] T. Bhatia *et al.*, “CMC Combustor Liner Demonstration in a Small Helicopter Engine,” in *Volume 1: Aircraft Engine; Ceramics; Coal, Biomass and Alternative Fuels; Education; Electric Power; Manufacturing Materials and Metallurgy*, Glasgow, UK: ASMEDC, Oct. 2010, pp. 509–513. doi: 10.1115/GT2010-23810.

[29] D. Tejero-Martin, C. Bennett, and T. Hussain, “A review on environmental barrier coatings: History, current state of the art and future developments,” *J. Eur. Ceram. Soc.*, vol. 41, no. 3, pp. 1747–1768, Mar. 2021, doi: 10.1016/j.jeurceramsoc.2020.10.057.

[30] C. Gatzen, D. E. Mack, O. Guillon, and R. Vaßen, “YAlO3—A Novel Environmental Barrier Coating for Al2O3/Al2O3–Ceramic Matrix Composites,” *Coatings*, vol. 9, no. 10, p. 609, Sept. 2019, doi: 10.3390/coatings9100609.

[31] M. Fritsch and H. Klemm, “The Water-Vapor hot Gas Corrosion Behavior of Al2O3-Y2O3 Materials, Y2Si05 and Y3Al5O12-Coated Alumina in a Combustion Environment,” in *Ceramic Engineering and Science Proceedings*, vol. 27, D. Zhu, U. Schulz, A. Wereszczak, and E. Lara-Curzio, Eds., Hoboken, NJ, USA: John Wiley & Sons, Inc., 2006, pp. 148–159. doi: 10.1002/9780470291320.ch14.

[32] M. Fritsch, *Heißgaskorrosion keramischer Werkstoffe in H2O-haltigen Rauchgasatmosphären*. in Kompetenzen in Keramik, no. 2. Stuttgart: Fraunhofer-IRB-Verl, 2008.

[33] K. N. Lee, “Special Issue: Environmental Barrier Coatings,” *Coatings*, vol. 10, no. 6, p. 512, May 2020, doi: 10.3390/coatings10060512.

[34] K. N. Lee, “Yb_2 Si_2 O_7 Environmental barrier coatings with reduced bond coat oxidation rates via chemical modifications for long life,” *J. Am. Ceram. Soc.*, vol. 102, no. 3, pp. 1507–1521, Mar. 2019, doi: 10.1111/jace.15978.

[35] K. N. Lee, J. I. Eldridge, and R. C. Robinson, “Residual Stresses and Their Effects on the Durability of Environmental Barrier Coatings for SiC Ceramics,” *J. Am. Ceram. Soc.*, vol. 88, no. 12, pp. 3483–3488, Dec. 2005, doi: 10.1111/j.1551-2916.2005.00640.x.

[36] E. J. Opila, J. L. Smialek, R. C. Robinson, D. S. Fox, and N. S. Jacobson, “SiC Recession Caused by SiO_2 Scale Volatility under Combustion Conditions: II, Thermodynamics and Gaseous-Diffusion Model,” *J. Am. Ceram. Soc.*, vol. 82, no. 7, pp. 1826–1834, July 1999, doi: 10.1111/j.1151-2916.1999.tb02005.x.

[37] E. J. Opila and R. E. Hann, “Paralinear Oxidation of CVD SiC in Water Vapor,” *J. Am. Ceram. Soc.*, vol. 80, no. 1, pp. 197–205, Jan. 1997, doi: 10.1111/j.1151-2916.1997.tb02810.x.

[38] K. N. Lee, D. S. Fox, and N. P. Bansal, “Rare earth silicate environmental barrier coatings for SiC/SiC composites and Si3N4 ceramics,” *J. Eur. Ceram. Soc.*, vol. 25, no. 10, pp. 1705–1715, Jan. 2005, doi: 10.1016/j.jeurceramsoc.2004.12.013.

[39] N. S. Jacobson, “Silica Activity Measurements in the Y_2O_3 – SiO_2 System and Applications to Modeling of Coating Volatility,” *J. Am. Ceram. Soc.*, vol. 97, no. 6, pp. 1959–1965, June 2014, doi: 10.1111/jace.12974.

[40] G. C. C. Costa and N. S. Jacobson, “Mass spectrometric measurements of the silica activity in the Yb2O3–SiO2 system and implications to assess the degradation of silicate-based coatings in combustion environments,” *J. Eur. Ceram. Soc.*, vol. 35, no. 15, pp. 4259–4267, Dec. 2015, doi: 10.1016/j.jeurceramsoc.2015.07.019.

[41] D. H. Olson *et al.*, “Evolution of microstructure and thermal conductivity of multifunctional environmental barrier coating systems,” *Mater. Today Phys.*, vol. 17, p. 100304, Mar. 2021, doi: 10.1016/j.mtphys.2020.100304.

[42] K. N. Lee, “Protective coatings for gas turbines,” in *The gas turbine handbook*, National Energy Technology Laboratory, Department of Energy, 2007, pp. 420–432.

[43] M. A. Carpenter, E. K. H. Salje, and A. Graeme-Barber, “Spontaneous strain as a determinant of thermodynamic properties for phase transitions in minerals,” *Eur. J. Mineral.*, vol. 10, no. 4, pp. 621–691, July 1998, doi: 10.1127/ejm/10/4/0621.

[44] J. Kimmel, J. Price, K. More, P. Tortorelli, E. Sun, and G. Linsey, “The Evaluation of CFCC Liners After Field Testing in a Gas Turbine – IV,” in *Volume 1: Turbo Expo 2003*, Atlanta, Georgia, USA: ASMEDC, Jan. 2003, pp. 657–667. doi: 10.1115/GT2003-38920.

[45] M. J. Lance, M. J. Ridley, K. A. Kane, and B. A. Pint, “Raman spectroscopic characterization of SiO_2 phase transformation and Si substrate stress relevant to EBC performance,” *J. Am. Ceram. Soc.*, vol. 106, no. 10, pp. 6205–6210, Oct. 2023, doi: 10.1111/jace.19190.

[46] K. N. Lee and M. van Roode, “Environmental barrier coatings enhance performance of SiC/SiC ceramic matrix composites,” *American Ceramic Society. American Ceramic Society Bulletin*, vol. 98, no. 3. American Ceramic Society, Columbus, pp. 46-, 2019.

[47] E. Bakan and R. Vaßen, “Oxidation kinetics of atmospheric plasma sprayed environmental barrier coatings,” *J. Eur. Ceram. Soc.*, vol. 42, no. 12, pp. 5122–5128, Sept. 2022, doi: 10.1016/j.jeurceramsoc.2022.05.003.

[48] J. W. Hutchinson and Z. Suo, “Mixed Mode Cracking in Layered Materials,” in *Advances in Applied Mechanics*, vol. 29, Elsevier, 1991, pp. 63–191. doi: 10.1016/S0065-2156(08)70164-9.

[49] M. Ridley, E. Garcia, K. Kane, S. Sampath, and B. Pint, “Environmental barrier coatings on enhanced roughness SiC: Effect of plasma spraying conditions on properties and performance,” *J. Eur. Ceram. Soc.*, vol. 43, no. 14, pp. 6473–6481, Nov. 2023, doi: 10.1016/j.jeurceramsoc.2023.06.049.

[50] E. Bakan and R. Vaßen, “Oxidation kinetics of atmospheric plasma sprayed environmental barrier coatings,” *J. Eur. Ceram. Soc.*, vol. 42, no. 12, pp. 5122–5128, Sept. 2022, doi: 10.1016/j.jeurceramsoc.2022.05.003.

[51] D. Pan, M. W. Chen, P. K. Wright, and K. J. Hemker, “Evolution of a diffusion aluminide bond coat for thermal barrier coatings during thermal cycling,” *Acta Mater.*, vol. 51, no. 8, pp. 2205–2217, May 2003, doi: 10.1016/S1359-6454(03)00014-4.

[52] J. Rösler, M. Bäker, and M. Volgmann, “Stress state and failure mechanisms of thermal barrier coatings: role of creep in thermally grown oxide,” *Acta Mater.*, vol. 49, no. 18, pp. 3659–3670, Oct. 2001, doi: 10.1016/S1359-6454(01)00283-X.

[53] A. Abdelgawad and K. Al-Athel, “Effect of TGO thickness, pores, and creep on the developed residual stresses in thermal barrier coatings under cyclic loading using SEM image-based finite element model,” *Ceram. Int.*, vol. 47, no. 14, pp. 20064–20076, July 2021, doi: 10.1016/j.ceramint.2021.03.336.

[54] J. Jiang, W. Wang, X. Zhao, Y. Liu, Z. Cao, and P. Xiao, “Numerical analyses of the residual stress and top coat cracking behavior in thermal barrier coatings under cyclic thermal loading,” *Eng. Fract. Mech.*, vol. 196, pp. 191–205, June 2018, doi: 10.1016/j.engfracmech.2018.04.031.

[55] J. Song, H. Qi, S. Li, X. Yang, D. Shi, and C. Fei, “A diffusion-coupled cohesive element model for cracking analysis of thermal barrier coatings,” *Eng. Fract. Mech.*, vol. 246, p. 107625, Apr. 2021, doi: 10.1016/j.engfracmech.2021.107625.

[56] S. Kyaw, A. Jones, and T. Hyde, “Predicting failure within TBC system: Finite element simulation of stress within TBC system as affected by sintering of APS TBC, geometry of substrate and creep of TGO,” *Eng. Fail. Anal.*, vol. 27, pp. 150–164, Jan. 2013, doi: 10.1016/j.engfailanal.2012.07.005.

[57] F. Sun, X. Fan, T. Zhang, P. Jiang, and J. Yang, “Numerical analysis of the influence of pore microstructure on thermal conductivity and Young’s modulus of thermal barrier coating,” *Ceram. Int.*, vol. 46, no. 15, pp. 24326–24332, Oct. 2020, doi: 10.1016/j.ceramint.2020.06.214.

[58] G. C. Gleason and J. Tullis, “A flow law for dislocation creep of quartz aggregates determined with the molten salt cell,” *Tectonophysics*, vol. 247, no. 1–4, pp. 1–23, July 1995, doi: 10.1016/0040-1951(95)00011-B.

[59] T. A. Taylor and C. R. Barrett, “Creep and recovery of silicon single crystals,” *Mater. Sci. Eng.*, vol. 10, pp. 93–102, Jan. 1972, doi: 10.1016/0025-5416(72)90073-0.

[60] C. H. Carter, R. F. Davis, and J. Bentley, “Kinetics and Mechanisms of High-Temperature Creep in Silicon Carbide: I, Reaction-Bonded,” *J. Am. Ceram. Soc.*, vol. 67, no. 6, pp. 409–417, June 1984, doi: 10.1111/j.1151-2916.1984.tb19726.x.

[61] Yong Yang, “RE_2SiO_5 (RE= Er, Gd, Y, Yb), Which is More Suitable for the Top-Coat of EBCs? A Problem Clarification via Finite Element Simulation Study,” *J. Ceram. Sci. Technol.*, no. 01, 2022, doi: 10.4416/JCST2021-00021.

[62] Y. Zhou, C. Zhao, F. Wang, Y. Sun, L. Zheng, and X. Wang, “Theoretical Prediction and Experimental Investigation on the Thermal and Mechanical Properties of Bulk β- $Yb_2Si_2O_7$,” *J. Am. Ceram. Soc.*, vol. 96, no. 12, pp. 3891–3900, Dec. 2013, doi: 10.1111/jace.12618.

[63] B. T. Richards, M. R. Begley, and H. N. G. Wadley, “Mechanisms of Ytterbium Monosilicate/Mullite/Silicon Coating Failure During Thermal Cycling in Water Vapor,” *J. Am. Ceram. Soc.*, vol. 98, no. 12, pp. 4066–4075, Dec. 2015, doi: 10.1111/jace.13792.

[64] R. Kassem and N. Al Nasiri, “A comprehensive study on the mechanical properties of Yb2SiO5 as a potential environmental barrier coating,” *Surf. Coat. Technol.*, vol. 426, p. 127783, Nov. 2021, doi: 10.1016/j.surfcoat.2021.127783.

[65] V. Hatty, H. Kahn, and A. H. Heuer, “Fracture Toughness, Fracture Strength, and Stress Corrosion Cracking of Silicon Dioxide Thin Films,” *J. Microelectromechanical Syst.*, vol. 17, no. 4, pp. 943–947, Aug. 2008, doi: 10.1109/JMEMS.2008.927069.

[66] D. H. Olson *et al.*, “Local thermal conductivity measurements to determine the fraction of α-cristobalite in thermally grown oxides for aerospace applications,” *Scr. Mater.*, vol. 177, pp. 214–217, Mar. 2020, doi: 10.1016/j.scriptamat.2019.10.027.

[67] C. Miehe, F. Welschinger, and M. Hofacker, “Thermodynamically consistent phase-field models of fracture: Variational principles and multi-field FE implementations,” *Int. J. Numer. Methods Eng.*, vol. 83, no. 10, pp. 1273–1311, Sept. 2010, doi: 10.1002/nme.2861.

[68] C. Miehe, M. Hofacker, and F. Welschinger, “A phase field model for rate-independent crack propagation: Robust algorithmic implementation based on operator splits,” *Comput. Methods Appl. Mech. Eng.*, vol. 199, no. 45–48, pp. 2765–2778, Nov. 2010, doi: 10.1016/j.cma.2010.04.011.

[69] C. Miehe, L.-M. Schänzel, and H. Ulmer, “Phase field modeling of fracture in multi-physics problems. Part I. Balance of crack surface and failure criteria for brittle crack propagation in thermo-elastic solids,” *Comput. Methods Appl. Mech. Eng.*, vol. 294, pp. 449–485, Sept. 2015, doi: 10.1016/j.cma.2014.11.016.